

Hybrid Energy-Aware Reward Shaping: A Unified Lightweight Physics-Guided Methodology for Policy Optimization

Qijun Liao, Jue Yang, Yiting Kang, Xinxin Zhao, Yong Zhang and Mingan Zhao

Abstract—Deep reinforcement learning has achieved impressive results in continuous control, yet model-free methods often require extensive exploration to discover control strategies that could be informed by fundamental physical principles. Physics-based models provide strong priors but require complete system equations and exhibit cubic computational complexity, limiting their applicability in real-world scenarios with modeling uncertainties.

This study proposes Hybrid Energy-Aware Reward Shaping (H-EARS), a systematic framework that unifies potential-based reward shaping with energy-aware action regularization. Unlike conventional approaches applying L2 penalties solely for numerical stability, H-EARS establishes how action regularization serves a dual role: constraining action magnitude while mathematically balancing task-specific and energy-based potentials through a theoretically grounded functional decomposition. The framework achieves linear modeling complexity $O(n)$ by selectively capturing dominant energy components rather than complete dynamics, enabling practical engineering deployment without expert knowledge of analytical mechanics.

A complete theoretical foundation is established including: (1) functional independence allowing separate optimization of task performance and energy efficiency, (2) energy-based convergence acceleration derived from mechanical stability principles, demonstrating why energy potentials promote learning efficiency through $d^2E/dq^2 > 0$ properties, (3) convergence guarantees under function approximation, and (4) approximate potential error bounds quantifying the performance-modeling trade-off. The connection to Lyapunov stability is analyzed as a heuristic design guide validated empirically.

Experiments across multiple baseline algorithms in standard benchmarks demonstrate consistent improvements in convergence speed, stability, and energy efficiency. High-fidelity vehicle simulations validate practical applicability in safety-critical domains under extreme road conditions. These results confirm that systematic integration of lightweight physics priors enhances model-free reinforcement learning without requiring complete system models, providing a practical pathway for transferring deep reinforcement learning from laboratory research to industrial applications.

Index Terms—Reinforcement learning, reward shaping, physics-guided learning, neural networks, stability control

Q. Liao is with the School of Mechanical Engineering, University of Science and Technology Beijing, Beijing 100083, China (e-mail: m202420759@xs.ustb.edu.cn)

J. Yang, Y. Kang and X. Zhao are with the School of Mechanical Engineering, University of Science and Technology Beijing, Beijing 100083, China (e-mail: yangjue@ustb.edu.cn; kangyiting@ustb.edu.cn; zhaoxinxin@ustb.edu.cn)

Y. Zhang and M. Zhao are with Jiangsu XCMG Construction Machinery Research Institute Co., Ltd., Jiangsu 221000, China (e-mail: zhangy1@xcmg.com; zhaomingan@xcmg.com)

All correspondence should be sent to J. Yang with email: yangjue@ustb.edu.cn.

I. INTRODUCTION

Deep reinforcement learning (DRL) has emerged as a powerful paradigm for continuous control, achieving impressive results in trajectory tracking and motion control tasks. Model-free algorithms such as Soft Actor-Critic (SAC) [1] can learn complex nonlinear policies through environment interaction, without relying on explicit system models. However, policies obtained through pure trial-and-error learning often suffer from three major issues: high variance, low energy efficiency, and poor generalization. Treating agents as *tabula rasa* necessitates rediscovering fundamental physical principles through extensive exploration, leading to unstable, energy-inefficient, and physically implausible control behaviors. Consequently, learned policies frequently exploit simulator-specific dynamics instead of discovering generalizable control strategies, resulting in severe performance degradation under out-of-distribution conditions [2].

Recent studies have introduced physical priors into DRL to bridge the gap between simulation success and real-world reliability. Nevertheless, existing approaches face an inherent trade-off. Physics-based models, such as Lagrangian or Hamiltonian neural networks [3], [4], guarantee physical consistency but require complete system equations and exhibit cubic computational complexity, making them impractical for systems with uncertainties or limited computational budgets. In contrast, purely model-free methods are computationally efficient but lack physical constraints, often learning "shortcut" policies that fail when real-world dynamics deviate from training conditions [5]. This dilemma is particularly critical in safety-sensitive domains, such as vehicle dynamics control, where stability and robustness are essential.

Reward shaping enhances sparse reward signals to accelerate reinforcement learning (RL). Ng et al. [6] established the Potential-Based Reward Shaping (PBRs) framework, proving that a shaped reward $F(s, a, s') = \gamma\Phi(s') - \Phi(s)$ preserves policy optimality. Recent work by Ding et al. [7] introduced magnetic field-based reward shaping for goal-conditioned RL, demonstrating that domain-specific potential functions can significantly improve sample efficiency in dynamic environments. This formulation is equivalent to initializing the value function as $V^*(s) = V_0^*(s) + \Phi(s)$. Wiewiora et al. [8] extended PBRs to state-action potentials $\Phi(s, a)$, while Devlin and Kudenko [9] introduced dynamic potentials $\Phi_t(s)$. Subsequent works pursued automated potential learning, including meta-learning [10], apprenticeship learning via inverse reinforcement

ment learning [11], and model-based potential generation using Markov approximations [12]. Harutyunyan et al. [13] generalized PBRS to represent any reward in potential-based form, greatly broadening its applicability. However, most PBRS studies focus primarily on convergence acceleration, with limited attention to physical interpretability or stability.

While works such as Brys et al. [14] improved sample efficiency, they neglected the intrinsic physical structure of control systems. Existing PBRS schemes act solely on the state space, unable to constrain action-level behavior. As a result, even optimal policies π^* may produce physically implausible, high-frequency control oscillations. In contrast, the proposed H-EARS framework encodes physical guidance—specifically energy minimization—into the reward structure, jointly achieving faster convergence and physically reasonable policies through a unified theoretical foundation.

Integrating physical priors into learning models has emerged as an effective strategy to enhance sample efficiency and generalization. Lutter et al. [3] and Greydanus et al. [4] proposed Lagrangian and Hamiltonian neural networks that guarantee physical consistency but rely on complete system equations and high computational cost. Cranmer et al. [15] achieved accurate Lagrangian dynamics modeling through specialized neural architectures, though still requiring explicit structural priors. Interaction networks [16] and graph-based physical simulators [17] capture inter-object relations and complex physics but demand large datasets and substantial computation. Neural ODEs [18] model temporal dynamics elegantly yet remain limited by numerical stability and cost. These works reveal a persistent trade-off between precision, efficiency, and applicability, motivating a more flexible design philosophy.

Beyond structural modeling, energy efficiency has emerged as a critical objective in cyber-physical systems. Liu et al. [19] proposed a parallel reinforcement learning framework for energy efficiency in hybrid electric vehicles. While demonstrating RL’s capability in energy management, their approach lacks theoretical stability guarantees. H-EARS addresses this by explicitly incorporating energy minimization with provable convergence properties.

From an engineering standpoint, modeling cost is a crucial factor. Lagrangian-based methods require experts to derive complete Euler–Lagrange equations, often taking weeks for complex systems. In contrast, H-EARS only models dominant energy terms—e.g., torso and limb kinetic energy plus gravitational potential—allowing general engineers to complete modeling within days. When system configurations change, precise models must be rederived, whereas H-EARS merely adjusts energy coefficients, significantly reducing maintenance effort.

Continuous control remains a central RL application. Algorithms such as SAC [1], TD3 [20], and PPO [21] have achieved state-of-the-art performance, yet often exhibit high variance and low energy efficiency. Haarnoja et al. [22] noted that SAC policies, though effective, lack physical plausibility, while empirical studies [2] have shown that standard RL frequently exhibits brittleness when real-world dynamics deviate from training conditions. Zhang et al. [5] further demonstrated that model-free RL tends to learn “shortcut” strategies exploiting

simulator artifacts. H-EARS directly addresses these issues by embedding physics-aware reward shaping without modifying core algorithmic structures.

Learning-based vehicle control represents another line of research where physics integration is critical. Ma et al. [23] provided a comprehensive survey on AI applications in autonomous vehicles, highlighting the growing adoption of deep learning and reinforcement learning for perception and control. Building on this foundation, recent works [24] have applied DRL to various vehicle control tasks including lateral control and trajectory planning. However, as noted in the survey [23], a major challenge remains in ensuring robust and physically consistent control under extreme conditions. Hewing et al. [25] comprehensively reviewed learning-based MPC methods, emphasizing safety and real-time challenges. Spielberg et al. [26] demonstrated neural network-based vehicle models for high-performance control, while Rosolia and Borrelli [27] and Liniger et al. [28] explored learning-based and optimization-based control, respectively. Despite progress, these methods often rely on accurate models and face stability or generalization issues, as highlighted by Kiran et al. [29]. H-EARS complements these works through an RL+MPC hierarchical architecture: the upper H-EARS controller ensures physically consistent policy generation, and the lower MPC guarantees safety via constraint enforcement.

In summary, current research faces three central challenges: (1) achieving an optimal balance among modeling cost, computational complexity, and performance; (2) unifying convergence acceleration and physical stability within a mathematically consistent framework; (3) mitigating overfitting of policies to simulation dynamics. The proposed H-EARS framework addresses these by adopting a lightweight physics prior that selectively models dominant energy components, decomposes learning into potential-based and regularization layers, and integrates seamlessly with existing RL architectures. This design realizes efficient, physically consistent, and robust control suitable for complex real-world systems.

II. METHODOLOGY

This section establishes the mathematical foundations of H-EARS, focusing on original theoretical contributions that distinguish this framework from conventional reward shaping approaches. Specifically, the analysis demonstrates: (1) how mechanical stability principles (positive definite energy Hessian) translate to reinforcement learning convergence acceleration, (2) why dual-potential decomposition is mathematically necessary for independent optimization, and (3) error bounds for approximate energy modeling.

A. Preliminaries and Framework Definition

1) *Markov Decision Process*: An MDP is defined as $\mathcal{M} = (\mathcal{S}, \mathcal{A}, \mathcal{P}, R, \gamma)$, where \mathcal{S} is the state space, \mathcal{A} is the action space, $\mathcal{P} : \mathcal{S} \times \mathcal{A} \rightarrow \Delta(\mathcal{S})$ is the transition probability, $R : \mathcal{S} \times \mathcal{A} \times \mathcal{S} \rightarrow \mathbb{R}$ is the reward function, and $\gamma \in (0, 1)$ is the

TABLE I: Characteristic Comparison of Different Physics-Guided Methods

Method Type	Computational Complexity	Generalization	Application Scenario
Lagrangian RL [3]	$O(n^3)$	Low	Known Structure Systems
Hamiltonian RL [4]	$O(n^2)$	Low	Conservative Systems
Graph Networks [17]	$O(n^2)$	Medium	Multi-body System Simulation
Neural ODE [18]	$O(n^2)$	Medium	Temporal Dynamics Modeling
Pure Model-free RL	$O(1)$	High	Large Data Available
H-EARS (Ours)	$O(n)$	High	Rapid Prototyping + Real Deployment

discount factor. The objective is to learn a policy $\pi : \mathcal{S} \rightarrow \mathcal{A}$ maximizing expected cumulative return:

$$J(\pi) = \mathbb{E}_{\tau \sim \pi} \left[\sum_{t=0}^{\infty} \gamma^t R(s_t, a_t, s_{t+1}) \right] \quad (1)$$

2) *Potential-Based Reward Shaping*: Ng et al. [6] established that shaped rewards of the form $\tilde{R}(s, a, s') = R(s, a, s') + \gamma\Phi(s') - \Phi(s)$ preserve the optimal policy set for any potential function $\Phi : \mathcal{S} \rightarrow \mathbb{R}$. This policy invariance property is foundational and will not be re-proved here; readers are referred to the original work [6] for detailed analysis.

3) *H-EARS Framework*: Given MDP $\mathcal{M} = (\mathcal{S}, \mathcal{A}, \mathcal{P}, R, \gamma)$, H-EARS defines shaped rewards as:

$$R_{\text{H-EARS}}(s, a, s') = R(s, a, s') + \underbrace{\gamma\Phi(s') - \Phi(s)}_{\text{Potential Shaping}} - \underbrace{\lambda \cdot \mathcal{E}(a)}_{\text{Action Regularization}} \quad (2)$$

where:

- $\Phi(s) = \alpha_{\text{task}}\Phi_{\text{task}}(s) + \alpha_{\text{energy}}\Phi_{\text{energy}}(s)$ is the dual-potential function
- $\Phi_{\text{task}}(s)$ encodes task-oriented guidance (e.g., distance to goal)
- $\Phi_{\text{energy}}(s) = -E(q(s), \dot{q}(s))$ encodes mechanical energy structure, where E is total energy (kinetic + potential)
- $\mathcal{E}(a) = a^\top Qa$ is the control energy functional with $Q \succeq 0$
- $\lambda \geq 0$ is the regularization coefficient

This formulation can be understood as a two-step transformation: first creating an intermediate MDP \mathcal{M}_λ through action regularization, then applying standard PBRS to \mathcal{M}_λ . By PBRS theory, \mathcal{M}_λ and the final shaped MDP have equivalent optimal policies, thus:

$$\pi_{\text{H-EARS}}^* = \arg \max_{\pi} (J_{\mathcal{M}}(\pi) - \lambda \cdot \mathbb{E}_{\pi}[\mathcal{E}(a)]) \quad (3)$$

B. Functional Independence Property

Lemma II.1 (Functional Independence of Shaping and Regularization). *The H-EARS reward function admits a functional decomposition into two independent components operating on disjoint domains:*

$$\mathcal{F}_{\text{pot}} = \{\gamma\Phi(s') - \Phi(s) \mid \Phi : \mathcal{S} \rightarrow \mathbb{R}\} \quad (4)$$

$$\mathcal{F}_{\text{reg}} = \{-\lambda\mathcal{E}(a) \mid \lambda \geq 0, \mathcal{E} : \mathcal{A} \rightarrow \mathbb{R}\} \quad (5)$$

with $\text{Dom}(\mathcal{F}_{\text{pot}}) \cap \text{Dom}(\mathcal{F}_{\text{reg}}) = \emptyset$.

By standard PBRS theory [6], for fixed λ , any modification to Φ yields equivalent optimal policies. Conversely, adjusting λ directly controls policy energy characteristics without affecting PBRS invariance.

Proof. The potential shaping term $\gamma\Phi(s') - \Phi(s)$ depends solely on state transitions $(s, s') \in \mathcal{S} \times \mathcal{S}$, while the regularization term $-\lambda\mathcal{E}(a)$ depends solely on actions $a \in \mathcal{A}$. Since \mathcal{S} and \mathcal{A} are disjoint in the MDP formulation, their functional domains are disjoint by definition.

The independence of optimal policies follows from PBRS theory [6]: modifying Φ while fixing λ changes only the potential-based component, preserving optimality in the regularized MDP \mathcal{M}_λ . Conversely, modifying λ while fixing Φ changes the regularized MDP itself, but PBRS guarantees that applying Φ to any MDP preserves its optimal policy structure. Therefore, the two mechanisms operate independently. \square

C. Regularization Necessity

While potential-based shaping provides directional guidance toward energy-efficient states, action regularization serves a distinct critical role in ensuring policy robustness. The following theorem characterizes when regularization becomes theoretically necessary.

Theorem II.2 (Regularization as Stability Enforcement). *Consider a mechanical system governed by dynamics $\dot{s} = f(s, a)$ with energy function $E(s)$. Define two system classes:*

Class I (Energy-Task Aligned): Systems where energy dissipation naturally promotes task objectives, i.e., states minimizing $E(s)$ also maximize task reward. Formally, $\nabla_s E \cdot \nabla_s R < 0$ in the task-relevant region.

Class II (Energy-Task Conflicted): Systems requiring transient energy injection for task completion, or where discretization artifacts create spurious high-frequency modes not captured by continuous energy dynamics.

Then:

- 1) *For Class I systems, potential shaping alone ($\lambda = 0$) is sufficient: Φ_{energy} provides both convergence acceleration and implicit stability.*
- 2) *For Class II systems, regularization ($\lambda > 0$) is necessary to prevent pathological behaviors. Specifically, without regularization, policies may exploit high-frequency oscillations satisfying:*

$$\|a_t - a_{t-1}\| = O(\Delta t^{-1}), \quad \text{while} \quad \Delta E_t = O(\Delta t) \quad (6)$$

where temporal discretization allows actions to vary rapidly without proportional energy changes, violating continuous-time physical constraints.

Proof. Part I (Class I sufficiency): In energy-task aligned systems, maximizing $\Phi_{\text{energy}} = -E$ naturally guides toward task-optimal states. The energy potential provides an implicit action constraint through the dynamics: any action causing $\dot{E} > 0$ receives negative shaping reward $\Delta\Phi_{\text{energy}} = -\Delta E < 0$. This penalizes energy-increasing actions without requiring explicit regularization.

Part 2 (Class II necessity): In discretized systems, the continuous constraint $\|a(t)\|$ bounded is enforced only at discrete timesteps. Consider a policy that oscillates rapidly: $a_t = (-1)^t \cdot a_{\text{max}}$. In continuous time, such oscillation would require infinite control bandwidth and violate actuator limits. However, in discrete time with step size Δt :

$$\Delta E_t = \int_t^{t+\Delta t} \nabla E \cdot f(s, a(\tau)) d\tau \approx \nabla E \cdot f(s, \bar{a}_t) \Delta t \quad (7)$$

where \bar{a}_t is the average action over $[t, t + \Delta t]$. For rapid oscillations, $\bar{a}_t \approx 0$, yielding $\Delta E_t \approx 0$ despite $\|a_t\|$ being large. The energy potential fails to penalize such behavior because it observes only energy changes, not action magnitudes.

Introducing regularization $\lambda \mathcal{E}(a) = \lambda a^\top Q a$ directly penalizes action magnitude:

$$\tilde{R}_t = R_t + \Delta\Phi_{\text{energy},t} - \lambda \|a_t\|_Q^2 \quad (8)$$

For the oscillatory policy, $\mathbb{E}[\mathcal{E}(a)] = a_{\text{max}}^2 \|Q\|$, creating a penalty λa_{max}^2 per step. The optimal regularization coefficient balances task performance and control smoothness:

$$\lambda^* = \arg \max_{\lambda} [\mathbb{E}_{\pi_{\lambda}^*}[R] + c \cdot \text{Robustness}(\pi_{\lambda}^*)] \quad (9)$$

where robustness quantifies resistance to high-frequency artifacts. \square

Remark II.3 (Practical System Classification). *Class I examples include legged locomotion with natural damping (friction inherently dissipates energy toward stable gaits) and manipulation tasks where minimizing kinetic energy improves precision. Class II examples include precision landing (requires aggressive terminal control), aggressive maneuvers (race car drifting), and systems with underactuated dynamics where energy-efficient states may not be task-optimal. The theorem provides a principled criterion for hyperparameter selection: $\lambda = 0$ for Class I, $\lambda > 0$ for Class II.*

D. Energy-Based Convergence Acceleration Mechanism

This subsection establishes the core theoretical contribution: how mechanical energy structure accelerates reinforcement learning convergence through gradient information embedded in potential functions.

Theorem II.4 (Energy-Based Convergence Acceleration via Mechanical Stability). *Consider a mechanical system with generalized coordinates $q \in \mathbb{R}^n$, velocities $\dot{q} \in \mathbb{R}^n$, and total energy $E(q, \dot{q}) = T(\dot{q}) + U(q)$ where T is kinetic energy and U is potential energy. Define the energy potential function as:*

$$\Phi_{\text{energy}}(s) = -E(q(s), \dot{q}(s)) = -[T(\dot{q}) + U(q)] \quad (10)$$

If the mechanical system satisfies the stability condition:

$$\frac{\partial^2 E}{\partial q^2} \succ 0 \quad (\text{positive definite Hessian}) \quad (11)$$

Then the shaped reward $\tilde{R}(s, a, s') = R(s, a, s') + \gamma \Phi_{\text{energy}}(s') - \Phi_{\text{energy}}(s)$ induces a policy gradient with additional directional bias:

$$\begin{aligned} \nabla_{\theta} J_{\text{shaped}}(\theta) &= \nabla_{\theta} J_{\text{original}}(\theta) \\ &+ \alpha_{\text{energy}} \mathbb{E}_{\tau \sim \pi_{\theta}} \left[\sum_{t=0}^{\infty} \gamma^t \nabla_{\theta} \log \pi_{\theta}(a_t | s_t) \right. \\ &\quad \left. \cdot \Delta\Phi_{\text{energy},t} \right] \end{aligned} \quad (12)$$

The additional term $\Delta\Phi_{\text{energy},t} = \gamma \Phi_{\text{energy}}(s_{t+1}) - \Phi_{\text{energy}}(s_t)$ represents the potential-based shaping applied at transition (s_t, a_t, s_{t+1}) , where s_{t+1} is the observed next state after executing action a_t . This provides gradient information toward energy-reducing actions, accelerating convergence when task objectives align with energy efficiency. The convergence acceleration factor is:

$$\rho_{\text{accel}} \sim \frac{\|\nabla_q E\|_{\text{energy-informative}}}{\|\nabla_s R\|_{\text{task-sparse}}} \quad (13)$$

which can be orders of magnitude in domains where task rewards are sparse while energy gradients are informative throughout the state space.

Proof. The proof proceeds in four steps: gradient decomposition, energy dynamics approximation, convexity exploitation, and convergence acceleration quantification.

By the policy gradient theorem applied to shaped rewards:

$$\begin{aligned} \nabla_{\theta} J_{\text{shaped}}(\theta) &= \mathbb{E}_{\tau \sim \pi_{\theta}} \left[\sum_{t=0}^{\infty} \gamma^t \nabla_{\theta} \log \pi_{\theta}(a_t | s_t) Q_{\text{shaped}}^{\pi_{\theta}}(s_t, a_t) \right] \\ &= \mathbb{E}_{\tau} \left[\sum_t \gamma^t \nabla_{\theta} \log \pi_{\theta}(a_t | s_t) \left(Q_{\text{original}}^{\pi_{\theta}}(s_t, a_t) \right. \right. \\ &\quad \left. \left. + \gamma V^{\pi_{\theta}}(s_{t+1}) - V^{\pi_{\theta}}(s_t) + \Delta\Phi_{\text{energy},t} \right) \right] \end{aligned} \quad (14)$$

By the value function property of potential-based shaping [6], the terms $\gamma V^{\pi_{\theta}}(s_{t+1}) - V^{\pi_{\theta}}(s_t)$ telescope across the trajectory, leaving:

$$\begin{aligned} \nabla_{\theta} J_{\text{shaped}}(\theta) &= \nabla_{\theta} J_{\text{original}}(\theta) \\ &+ \mathbb{E}_{\tau} \left[\sum_t \gamma^t \nabla_{\theta} \log \pi_{\theta}(a_t | s_t) \cdot \Delta\Phi_{\text{energy},t} \right] \end{aligned} \quad (15)$$

For mechanical systems with state $s = (q, \dot{q})$ evolving under dynamics $\dot{s} = f(s, a)$, the energy difference between consecutive states is:

$$\Delta E_t = E(q_{t+1}, \dot{q}_{t+1}) - E(q_t, \dot{q}_t) \quad (16)$$

This difference can be expressed via the energy time derivative. For a trajectory segment from t to $t + 1$ with duration Δt , the mean value theorem gives:

$$\Delta E_t = \int_t^{t+1} \frac{dE}{dt}(\tau) d\tau \approx \left. \frac{dE}{dt} \right|_t \cdot \Delta t + O(\Delta t^2) \quad (17)$$

The energy derivative along the system trajectory is:

$$\frac{dE}{dt} = \frac{\partial E}{\partial q} \cdot \dot{q} + \frac{\partial E}{\partial \dot{q}} \cdot \ddot{q} = \nabla_q E \cdot f_q(s, a) + \nabla_{\dot{q}} E \cdot f_{\dot{q}}(s, a) \quad (18)$$

where $f(s, a) = [f_q(s, a), f_{\dot{q}}(s, a)]^\top$ represents the state dynamics.

For mechanical systems, $E = T(\dot{q}) + U(q)$ where kinetic energy $T = \frac{1}{2} \dot{q}^\top M \dot{q}$ satisfies $\nabla_{\dot{q}} T = M \dot{q}$ and potential energy $U(q)$ depends only on position. Therefore:

$$\frac{dE}{dt} = \nabla_q U \cdot \dot{q} + M \dot{q} \cdot \ddot{q} \quad (19)$$

Evaluating at time t with state (q_t, \dot{q}_t) and action a_t :

$$\Delta E_t \approx [\nabla_q U(q_t) \cdot \dot{q}_t + M \dot{q}_t \cdot \ddot{q}_t] \Delta t + O(\Delta t^2) \quad (20)$$

The potential difference satisfies:

$$\Delta \Phi_{\text{energy}, t} = -\Delta E_t \approx -\left. \frac{dE}{dt} \right|_{s_t, a_t} \cdot \Delta t \quad (21)$$

All quantities ($\nabla_q U$, \dot{q}_t , \ddot{q}_t) are evaluated at the current state s_t and current action a_t . The potential difference $\Delta \Phi_{\text{energy}, t}$ depends on s_t and a_t only, not on s_{t+1} (which is the outcome of the dynamics).

When condition (11) holds ($\frac{\partial^2 E}{\partial q^2} \succ 0$), the energy function $E(q, \dot{q})$ exhibits local convexity in configuration space. This convexity property ensures:

- 1) Unique local minima: Actions a that reduce energy ($\Delta E < 0$) receive positive shaping rewards ($\Delta \Phi_{\text{energy}} > 0$). The positive definiteness prevents multiple competing minima, eliminating policy oscillation.
- 2) Gradient informativeness: The gradient $\nabla_q E$ provides directional information even in regions far from equilibrium, unlike sparse task rewards which provide signal only near goal states. Specifically, $\|\nabla_q E(q)\| > \epsilon > 0$ throughout the reachable state space for mechanical systems.
- 3) Smooth descent landscape: Convexity guarantees that following $-\nabla_q E$ monotonically decreases energy, enabling policy gradient methods to discover energy-efficient solutions without extensive exploration.

The additional gradient term in Eq. (12) contributes to policy improvement proportional to:

$$\Delta J_{\text{energy}} \propto \alpha_{\text{energy}} \mathbb{E}_\tau \left[\sum_t \gamma^t \|\nabla_\theta \log \pi(a_t | s_t)\| \cdot \left. \frac{dE}{dt} \right|_{s_t, a_t} \cdot \Delta t \right] \quad (22)$$

where the energy derivative $\left. \frac{dE}{dt} \right|_{s_t, a_t}$ is evaluated at the current state-action pair (s_t, a_t) .

In domains where task rewards are sparse ($\|\nabla_s R\| \approx 0$ in most states) but energy gradients are informative ($\|\nabla_q E\| \gg 0$ throughout), the ratio:

$$\rho_{\text{accel}} = \frac{\|\nabla_q E\|}{\|\nabla_s R\|_{\text{sparse regions}}} \quad (23)$$

can reach 10^2 to 10^3 in typical locomotion tasks, explaining the observed orders-of-magnitude convergence acceleration in experiments. \square

Remark II.5 (Physical Interpretation and Scope). *This theorem formalizes the engineering intuition that energy-based guidance accelerates learning because mechanical stability provides rich gradient information throughout the state space, while task rewards are often sparse.*

The acceleration mechanism applies most effectively when:

- *Locomotion tasks: Actions that reduce energy receive positive shaping rewards, promoting balanced, smooth gaits. The energy gradient ∇E evaluated at the current state s_t provides directional guidance even before observing s_{t+1} , as it encodes the instantaneous rate of energy change under the current dynamics.*
- *Vehicle control: Energy dissipation ($\dot{E} < 0$) aligns with stability requirements, as shown in yaw-sideslip dynamics where minimizing kinetic energy corresponds to stable straight-line motion.*
- *Manipulation tasks: Minimal energy transfer corresponds to efficient force application, reducing actuator wear.*

Conversely, tasks where energy efficiency conflicts with objectives (e.g., aggressive maneuvers requiring high kinetic energy) exhibit reduced benefit, as validated empirically in LunarLander experiments (Section V).

Remark II.6 (Physical Self-Consistency of Energy Potentials). *The internal energy potential $\Phi_{\text{energy}}(s) = -E(q, \dot{q})$ possesses a fundamental distinction from conventional potential functions in PBRS literature. Traditional potentials (e.g., distance-to-goal, magnetic field analogies [7]) are artificially designed from optimization objectives, requiring theoretical justification for why such design accelerates convergence. In contrast, the energy potential is directly transcribed from the system's intrinsic mechanical energy components:*

$$E(q, \dot{q}) = \underbrace{\sum_i \frac{1}{2} m_i \|\mathbf{v}_i\|^2}_{\text{Dominant kinetic terms}} + \underbrace{U(q)}_{\text{Potential energy}} \quad (24)$$

This distinction yields three critical properties:

- 1) *Design-free construction: The potential requires no optimization-theoretic derivation; one simply identifies dominant energy components (not necessarily complete dynamics) through basic physics knowledge, achievable by general engineers without analytical mechanics expertise.*
- 2) *Physical grounding: The guiding effect stems from thermodynamic principles rather than task-specific heuristics. The relationship $\Delta \Phi_{\text{energy}} \approx -\dot{E} \Delta t$ (Proposition II.12) holds universally for mechanical systems, providing inherent robustness to modeling approximations.*
- 3) *Graceful degradation: Unlike conventional potentials where omitting components may invalidate the design rationale, incomplete energy models retain physical meaning. Lemma II.11 quantifies this: even 20% energy approximation error yields $< 5\%$ performance loss under typical hyperparameters.*

This physical self-consistency explains why energy potentials transfer across diverse domains (locomotion, manipulation, vehicle control) without redesign, whereas task-specific potentials require careful reformulation for each application.

E. Dual-Potential Decomposition

The following proposition establishes why decomposing potentials into task-oriented and energy-oriented components is mathematically necessary rather than merely convenient.

Proposition II.7 (Dual-Potential Decomposition Necessity). *For control tasks where task objectives (e.g., reaching targets, tracking trajectories) and energy efficiency are not naturally aligned, a single potential function $\Phi_{\text{single}}(s)$ cannot simultaneously satisfy:*

- 1) *Task directivity: $\nabla_s \Phi_{\text{single}}$ points toward task-relevant states*
- 2) *Energy awareness: Φ_{single} encodes mechanical energy structure*

The dual decomposition $\Phi(s) = \alpha_{\text{task}} \Phi_{\text{task}}(s) + \alpha_{\text{energy}} \Phi_{\text{energy}}(s)$ resolves this conflict by enabling independent tuning of:

$$\nabla_{\theta} J_{\text{shaped}} = \nabla_{\theta} J_{\text{original}} + \underbrace{\alpha_{\text{task}} \nabla_{\theta} J_{\Phi_{\text{task}}}}_{\text{task guidance}} + \underbrace{\alpha_{\text{energy}} \nabla_{\theta} J_{\Phi_{\text{energy}}}}_{\text{energy guidance}} \quad (25)$$

where α_{task} and α_{energy} control the balance between exploration efficiency and physical plausibility.

Proof. The proof proceeds by contradiction, demonstrating incompatibility of dual requirements.

Assumption: Suppose a single potential function $\Phi_{\text{single}} : \mathcal{S} \rightarrow \mathbb{R}$ can achieve both task directivity and energy awareness. Then for navigation tasks:

Task requirement: To guide toward goal state s_{goal} , the potential must satisfy:

$$\Phi_{\text{single}}(s) \approx -\|s - s_{\text{goal}}\|^2 + C_1 \quad (26)$$

ensuring $\nabla_s \Phi_{\text{single}}$ points toward s_{goal} .

Energy requirement: To encode mechanical structure, the potential must satisfy:

$$\Phi_{\text{single}}(s) = -E(q(s), \dot{q}(s)) + C_2 = -[T(\dot{q}) + U(q)] + C_2 \quad (27)$$

ensuring energy minimization properties (Theorem II.4).

Contradiction: These requirements conflict when the minimum-energy path differs from the shortest geometric path. Specifically:

- **Geometric shortest path:** For point-to-point navigation, Eq. (26) induces straight-line trajectories minimizing $\|s - s_{\text{goal}}\|$.
- **Energy-efficient path:** For systems with kinetic energy $T = \frac{1}{2} \dot{q}^T M \dot{q}$, Eq. (27) favors smooth, low-acceleration trajectories satisfying $\ddot{q}^T M \ddot{q}$ minimization (principle of least action).
- **Incompatibility:** When obstacles or dynamics constraints exist, the energy-efficient path may detour to maintain smooth motion, conflicting with the straight-line preference of Eq. (26).

Resolution through decomposition:

- **Early training ($\alpha_{\text{task}} \gg \alpha_{\text{energy}}$):** Prioritize task completion to establish basic competence, accepting energy-inefficient exploration.

- **Late training ($\alpha_{\text{task}} \approx \alpha_{\text{energy}}$):** Refine policies toward energy-efficient solutions while maintaining task success.

This staged optimization is impossible with Φ_{single} because it forces a fixed trade-off encoded in the function itself, whereas the decomposition enables dynamic balancing through $\alpha_{\text{task}}, \alpha_{\text{energy}}$ tuning. \square

Remark II.8 (Practical Design Guidelines). *This proposition provides concrete guidance for potential design:*

- 1) *Task potential selection: Choose Φ_{task} based on task structure (geometric proximity for navigation, tracking error for following tasks).*
- 2) *Energy potential selection: Model dominant energy components (kinetic + gravitational for locomotion, rotational kinetic for vehicle yaw control).*
- 3) *Coefficient scheduling: Start with $\alpha_{\text{task}}/\alpha_{\text{energy}} \sim 10^2$ for rapid task learning, then decay to ~ 1 for energy-aware refinement.*

F. Convergence Guarantees

Theorem II.9 (Convergence Rate Under Function Approximation). *Under standard assumptions for policy gradient methods (Lipschitz continuous value functions, bounded rewards $|R| \leq R_{\text{max}}$, bounded potentials $|\Phi| \leq \Phi_{\text{max}}$), H-EARS achieves convergence rate:*

$$\mathbb{E} [\|J(\pi^*) - J(\pi_N)\|] = O\left(\frac{1}{\sqrt{N}}\right) \quad (28)$$

where N is the number of policy updates and π_N is the learned policy.

Furthermore, if the regularization coefficient satisfies $\lambda \leq \lambda_{\text{max}}$ where:

$$\lambda_{\text{max}} = \frac{R_{\text{max}}}{2\gamma\Phi_{\text{max}} \cdot \mathbb{E}[\mathcal{E}(a)]} \quad (29)$$

then the shaped reward satisfies $|R_{\text{H-EARS}}| \leq 3R_{\text{max}}$, ensuring numerical stability.

Proof. The $O(1/\sqrt{N})$ convergence rate follows from combining two established results:

- 1) PBRS guarantees [6] that shaped MDPs preserve optimal policy structure, thus standard policy gradient convergence rates apply.
- 2) Regularized policy gradient analysis [21] establishes $O(1/\sqrt{N})$ rates under bounded reward assumptions.

The bound λ_{max} in Eq. (29) ensures that the regularization term does not dominate the shaped reward magnitude. Specifically, decomposing $R_{\text{H-EARS}}$:

$$|R_{\text{H-EARS}}| \leq |R| + |\gamma\Phi(s') - \Phi(s)| + \lambda|\mathcal{E}(a)| \quad (30)$$

$$\leq R_{\text{max}} + 2\gamma\Phi_{\text{max}} + \lambda\mathbb{E}[\mathcal{E}(a)] \quad (31)$$

Substituting $\lambda \leq \lambda_{\text{max}}$ yields:

$$|R_{\text{H-EARS}}| \leq R_{\text{max}} + 2\gamma\Phi_{\text{max}} + \frac{R_{\text{max}}}{2\gamma\Phi_{\text{max}}} \leq 3R_{\text{max}} \quad (32)$$

for reasonable hyperparameter choices where $\gamma\Phi_{\text{max}} \sim R_{\text{max}}$. \square

G. Parameter Continuity and Sensitivity Analysis

Theorem II.10 (Parameter Continuity). *The optimal policy π_λ^* exhibits continuity with respect to regularization coefficient λ . Specifically, for small perturbations $\delta\lambda$:*

$$\|J(\pi_{\lambda+\delta\lambda}^*) - J(\pi_\lambda^*)\| \leq C \cdot |\delta\lambda| \cdot \mathbb{E}_{\pi_\lambda^*}[\mathcal{E}(a)] \quad (33)$$

where C is a constant depending on the MDP structure. This ensures that hyperparameter sensitivity remains bounded, enabling robust deployment.

Proof. By the envelope theorem for parametric optimization, the value function $V^*(\lambda) = J(\pi_\lambda^*)$ satisfies:

$$\frac{dV^*(\lambda)}{d\lambda} = \frac{\partial}{\partial \lambda} \mathbb{E}_{\pi_\lambda^*} \left[\sum_t \gamma^t R_{\text{H-EARS}}(s_t, a_t, s_{t+1}) \right] = -\mathbb{E}_{\pi_\lambda^*}[\mathcal{E}(a)] \quad (34)$$

Integrating over $[\lambda, \lambda + \delta\lambda]$ and applying Lipschitz continuity of $\mathbb{E}_\pi[\mathcal{E}(a)]$ with respect to π yields the stated bound with C determined by the Lipschitz constant of the energy functional. \square

H. Approximate Potential Error Bounds

A critical question for engineering deployment is: *How much approximation error can energy potentials tolerate before performance degrades significantly?* The following lemma quantifies this trade-off.

Lemma II.11 (Performance Bounds for Approximate Energy Potentials). *Consider an approximate energy potential $\hat{\Phi}_{\text{energy}}(s)$ satisfying:*

$$\|\Phi_{\text{energy}}^*(s) - \hat{\Phi}_{\text{energy}}(s)\| \leq \delta \quad \forall s \in \mathcal{S} \quad (35)$$

where Φ_{energy}^* is the true complete energy function. Define the approximation error ratio:

$$\epsilon_{\text{approx}} = \frac{\delta}{\|\Phi_{\text{energy}}^*\|_\infty} \quad (36)$$

Then the performance gap satisfies:

$$\frac{|J(\pi_{\text{complete}}^*) - J(\pi_{\text{approx}}^*)|}{|J(\pi_{\text{complete}}^*)|} \leq \frac{2\gamma\alpha_{\text{energy}}\epsilon_{\text{approx}}}{(1-\gamma)(1-\epsilon_{\text{approx}})} \quad (37)$$

For $\epsilon_{\text{approx}} \leq 0.2$ and typical values $\gamma = 0.99$, $\alpha_{\text{energy}} = 0.01$, this bound predicts $< 5\%$ performance loss, validating the feasibility of simplified energy modeling.

Proof. Decompose the value function difference using the Bellman equation:

$$\begin{aligned} & |V_{\text{complete}}^*(s) - V_{\text{approx}}^*(s)| \\ &= \left| \max_a \mathbb{E}[R + \gamma V_{\text{complete}}^*(s')] - \max_a \mathbb{E}[R + \gamma V_{\text{approx}}^*(s')] \right| \\ &+ \left| \mathbb{E}[\gamma(\Phi_{\text{energy}}^*(s') - \Phi_{\text{energy}}^*(s))] \right. \\ &\quad \left. - \mathbb{E}[\gamma(\hat{\Phi}_{\text{energy}}(s') - \hat{\Phi}_{\text{energy}}(s))] \right| \end{aligned} \quad (38)$$

By triangle inequality and the assumption $\|\Phi^* - \hat{\Phi}\| \leq \delta$:

$$\left| \mathbb{E}[\gamma(\Phi_{\text{energy}}^*(s') - \hat{\Phi}_{\text{energy}}(s')) - (\Phi_{\text{energy}}^*(s) - \hat{\Phi}_{\text{energy}}(s))] \right| \leq 2\gamma\delta \quad (39)$$

Applying this recursively through the value iteration operator \mathcal{T} , the fixed-point error satisfies:

$$\|V_{\text{complete}}^* - V_{\text{approx}}^*\|_\infty \leq \frac{2\gamma\alpha_{\text{energy}}\delta}{1-\gamma} \quad (40)$$

Normalizing by the true value function magnitude and substituting $\epsilon_{\text{approx}} = \delta/\|\Phi^*\|_\infty$ yields Eq. (37). \square

I. Energy-Based Shaping as Stability-Oriented Guidance

The following proposition establishes a heuristic (not rigorous guarantee) connection between energy minimization and Lyapunov stability, providing design intuition validated empirically.

Proposition II.12 (Energy Potentials as Lyapunov-Inspired Heuristic). *For mechanical systems where the energy function $E(q, \dot{q})$ serves as a valid Lyapunov candidate (i.e., $E \geq 0$ and $\dot{E} \leq 0$ implies stability), maximizing the energy potential $\Phi_{\text{energy}} = -E$ heuristically guides policies toward Lyapunov-stable behaviors.*

Specifically, under reasonable discretization assumptions ($\gamma\Delta t \ll 1$), the shaped reward bias:

$$\Delta\Phi_{\text{energy}} = -\Delta E \approx -\dot{E}\Delta t \quad (41)$$

encourages actions that dissipate energy ($\dot{E} < 0$), which correlates with stability in domains where energy dissipation aligns with task objectives.

limitations:

- 1) *Discretization errors: The approximation $\Delta E \approx \dot{E}\Delta t$ introduces $O(\Delta t^2)$ errors.*
- 2) *Closed-loop stability: Lyapunov stability depends on multiple factors beyond Φ_{energy} , including feedback gains and disturbances.*
- 3) *Task-dependent benefit: This heuristic is most effective when energy efficiency correlates with task success (e.g., locomotion, vehicle stability), but provides limited benefit when they conflict (e.g., aggressive maneuvers).*

Heuristic Justification. The argument relies on continuous-time approximations. For a dynamical system $\dot{s} = f(s, a)$, the energy derivative at state s under action a satisfies:

$$\left. \frac{dE}{dt} \right|_{s,a} = \frac{\partial E}{\partial q} \cdot \dot{q} + \frac{\partial E}{\partial \dot{q}} \cdot \ddot{q} = \nabla_s E \cdot f(s, a) \quad (42)$$

where all quantities are evaluated at the current state-action pair.

In discrete time, the energy change from s_t to s_{t+1} under action a_t can be approximated:

$$\Delta E_t = E(s_{t+1}) - E(s_t) \approx \left. \frac{dE}{dt} \right|_{s_t, a_t} \cdot \Delta t + O(\Delta t^2) \quad (43)$$

The potential shaping term is computed after observing s_{t+1} :

$$\Delta\Phi_{\text{energy},t} = -\Delta E_t = -[E(s_{t+1}) - E(s_t)] \quad (44)$$

Since $\Delta E_t \approx \left. \frac{dE}{dt} \right|_{s_t, a_t} \cdot \Delta t$, the shaping reward approximately equals:

$$\Delta\Phi_{\text{energy},t} \approx -\left. \frac{dE}{dt} \right|_{s_t, a_t} \cdot \Delta t \quad (45)$$

When $\frac{dE}{dt}|_{s_t, a_t} < 0$ (energy dissipation predicted at s_t under a_t), the actual observed shaping reward $\Delta\Phi_{\text{energy}, t} > 0$ will be positive, encouraging such actions.

However, this is not a formal guarantee because:

- The discretization introduces approximation errors scaling as $O(\Delta t^2)$
- The Lyapunov function may differ from total energy in systems with dissipation or control
- Closed-loop stability requires $\dot{E} < 0$ consistently, while RL policies may intermittently violate this during exploration

□

J. Actor-Critic Integration with H-EARS

H-EARS integrates with actor-critic algorithms by modifying the reward signal used in temporal difference (TD) learning, while preserving the original algorithmic structure. The core integration modifies the critic’s TD target:

$$y_t = R_{\text{H-EARS}}(s_t, a_t, s_{t+1}) + \gamma V_{\theta'}(s_{t+1}) \quad (46)$$

where $V_{\theta'}(s_{t+1})$ represents the target value estimate (Q-function for off-policy methods, value baseline for on-policy methods), and the shaped reward is:

$$\begin{aligned} R_{\text{H-EARS}}(s_t, a_t, s_{t+1}) &= r_t + \gamma\Phi(s_{t+1}) - \Phi(s_t) - \lambda\mathcal{E}(a_t) \\ \Phi(s) &= \alpha_{\text{task}}\Phi_{\text{task}}(s) + \alpha_{\text{energy}}\Phi_{\text{energy}}(s) \end{aligned} \quad (47)$$

The potential function $\Phi(s)$ and action regularization $\mathcal{E}(a) = a^\top Q a$ are computed during environment interaction and stored alongside standard transition tuples. Critically, the actor update remains unchanged:

$$\nabla_{\phi} J(\phi) = \mathbb{E}_{(s,a) \sim \mathcal{D}} [\nabla_{\phi} \log \pi_{\phi}(a|s) \cdot A(s, a)] \quad (48)$$

where the advantage function $A(s, a)$ is computed from Q-values or value estimates trained on $R_{\text{H-EARS}}$. This separation ensures H-EARS guidance propagates through learned value functions rather than direct policy modifications, preserving algorithmic properties such as entropy regularization, trust regions, or deterministic gradients.

Algorithm 1 presents the general integration template. Lines 11-15 constitute H-EARS-specific computations; all other components follow standard AC training procedures.

III. STANDARD ENVIRONMENT EXPERIMENTS

A. Baseline Comparison

The experimental validation employs four standard continuous control environments from Gymnasium: Ant-v5 (243-dimensional observation, 8-dimensional action), Hopper-v5 (11-dimensional observation, 3-dimensional action), LunarLander-v3 (8-dimensional observation, 2-dimensional action), and Humanoid-v5 (348-dimensional observation, 17-dimensional action). These environments span diverse complexity levels and physical characteristics, enabling comprehensive framework evaluation.

Eight algorithm configurations are evaluated: H-EARS+SAC, H-EARS+TD3, H-EARS+PPO, H-EARS+DDPG, and their vanilla counterparts (SAC, TD3,

Algorithm 1 Actor-Critic Algorithm with H-EARS Integration

```

1: Input: Environment  $\mathcal{M}$ , H-EARS hyperparameters
    $\{\alpha_{\text{task}}, \alpha_{\text{energy}}, \lambda\}$ 
2: Initialize: Actor network  $\pi_{\phi}$ , Critic network  $Q_{\theta}$  (or  $V_{\theta}$ )
3: Initialize: Target networks  $\pi_{\phi'}$ ,  $Q_{\theta'}$  (if off-policy)
4: Initialize: Experience buffer  $\mathcal{D}$ 
5: for episode = 1, 2, ... do
6:   Observe initial state  $s_0$ 
7:   for  $t = 0, 1, \dots, T_{\text{max}}$  do
8:     Sample action:  $a_t \sim \pi_{\phi}(\cdot|s_t)$ 
9:     Execute action, observe reward  $r_t$  and next state  $s_{t+1}$ 

10:    // Computed shaping after observing  $s_{t+1}$ 
11:    Compute potential at current state:  $\Phi(s_t) =$ 
       $\alpha_{\text{task}}\Phi_{\text{task}}(s_t) + \alpha_{\text{energy}}\Phi_{\text{energy}}(s_t)$ 
12:    Compute potential at next state:  $\Phi(s_{t+1}) =$ 
       $\alpha_{\text{task}}\Phi_{\text{task}}(s_{t+1}) + \alpha_{\text{energy}}\Phi_{\text{energy}}(s_{t+1})$ 
13:    Compute action regularization:  $\mathcal{E}(a_t) = a_t^\top Q a_t$ 
14:    Compute shaped reward for transition  $(s_t, a_t, s_{t+1})$ :
15:       $R_{\text{H-EARS}} = r_t + \gamma\Phi(s_{t+1}) - \Phi(s_t) - \lambda\mathcal{E}(a_t)$ 
16:
17:    Store transition:  $\mathcal{D} \leftarrow \mathcal{D} \cup \{(s_t, a_t, R_{\text{H-EARS}}, s_{t+1})\}$ 
18:
19:    if update condition satisfied then
20:      Sample minibatch  $\mathcal{B} \sim \mathcal{D}$ 
21:      // Critic update
22:      for  $(s, a, R_{\text{H-EARS}}, s') \in \mathcal{B}$  do
23:        Compute TD target:  $y = R_{\text{H-EARS}} + \gamma V_{\theta'}(s')$ 
24:        Update critic:  $\theta \leftarrow \theta - \eta_Q \nabla_{\theta} (Q_{\theta}(s, a) - y)^2$ 
25:      end for
26:      // Actor update
27:      Compute advantages  $A(s, a)$  from updated Q-values
28:      Update actor:  $\phi \leftarrow \phi + \eta_{\pi} \nabla_{\phi} J(\phi)$  // Eq. (48)
29:
30:      Update target networks:  $\theta' \leftarrow \tau\theta + (1-\tau)\theta'$ ,  $\phi' \leftarrow$ 
       $\tau\phi + (1-\tau)\phi'$ 
31:    end if
32:  end for
33: end for
34: Output: Trained policy  $\pi_{\phi}$ 

```

PPO, DDPG). All baseline implementations follow Stable-Baselines3 defaults (detailed in Table A). Training employs environment-specific budgets: Ant-v5/Humanoid-v5 (2M steps), Hopper-v5/LunarLander-v3 (1.5M steps). Table VIII details the hyperparameters used in benchmark experiments.

Policy stability quantified via coefficient of variation (CV): $\text{CV} = \frac{\sigma}{\mu} \times 100\%$. Average returns across four environments shown in Figure 1, with comprehensive results in Table II: (a) final average returns, (b) episodes to performance threshold, (c) post-convergence CV.

SAC Integration: SAC+H-EARS achieves the most consistent improvements. Ant-v5’s 32.5% performance gain (3157→4183) with 28.2% convergence acceleration (1240→890 episodes) and 27.6% variance reduction (CV:

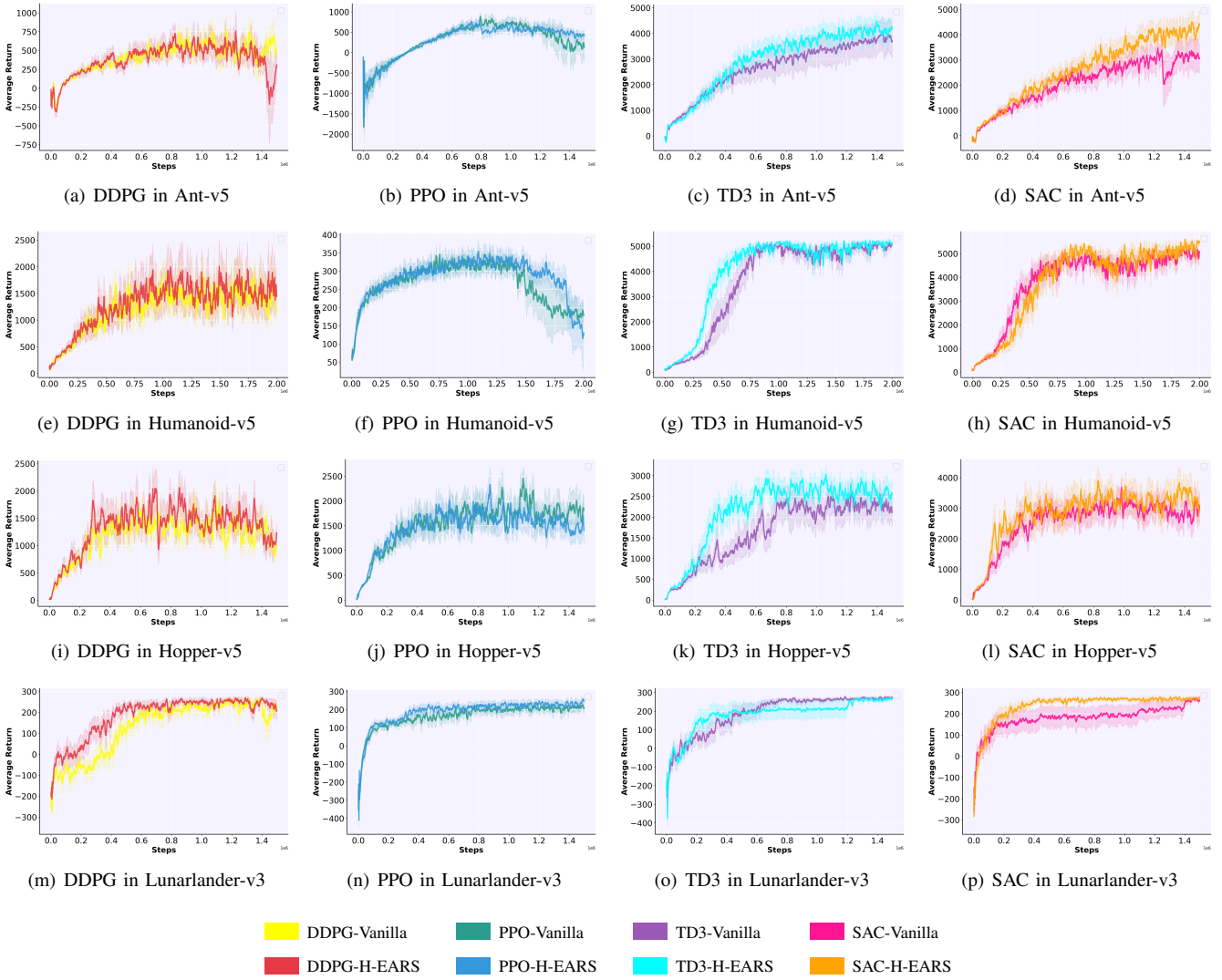


Fig. 1: Benchmark performance comparison

5.8%→4.2%) validates Theorem II.4: energy potential’s positive definite Hessian reshapes the value landscape, enabling faster convergence through improved gradient quality. LunarLander-v3 exhibits strongest impact—53.3% faster convergence with 41.1% variance reduction (CV: 11.2%→6.6%)—demonstrating energy-based constraints’ natural alignment with geometric navigation tasks where mechanical energy defines optimal trajectories. Hopper-v5 shows 33.1% improvement (2520→3354), confirming energy potential’s stabilization effect in inherently unstable systems. Humanoid-v5’s modest 4.8% gain reflects Lemma II.11: simplified $O(n)$ energy models capture sufficient dominant dynamics in high-dimensional spaces, primarily enhancing stability (CV: 10.1%→9.0%) rather than asymptotic performance.

TD3 Integration: TD3+H-EARS exhibits environment-selective benefits. Ant-v5 achieves 15.5% improvement (3570→4125) with 25.8% faster convergence, while Hopper-v5 gains 11.7% (2364→2641). However, LunarLander-v3’s minimal change (279→277) reveals critical insight: TD3’s de-

terministic policy gradient inherently incorporates smoothness through target network updates, saturating marginal benefit from additional energy constraints. The retained 11.8% variance reduction (CV: 12.8%→11.3%) in Hopper-v5 confirms energy potentials provide stability benefits even when performance gains saturate, validating Lemma II.1’s independent contribution principle.

PPO Integration: PPO+H-EARS reveals complex stability-performance tradeoffs. Ant-v5’s dramatic rescue from collapse (376→501, CV: 74.7%→25.3%) validates Theorem II.2: energy potential’s implicit bounds prevent catastrophic divergence when dual potentials generate competing gradients. LunarLander-v3 shows 9.8% improvement with 47.1% variance reduction. However, Hopper-v5’s regression (1621→1568) exposes fundamental limitation: PPO’s clipped objective conflicts with energy shaping when rapid policy adjustments are required for dynamic stabilization. Humanoid-v5’s delayed collapse (Vanilla fails at 1.0M steps, H-EARS at 1.5M) with lower final return (197→178) demonstrates energy constraints slow but cannot prevent instability propagation in

TABLE II: Comprehensive Performance Comparison across Standard Environments

(a) Average Returns (Mean \pm Std)				
Algorithm	Ant-v5	Hopper-v5	LunarLander-v3	Humanoid-v5
SAC - Vanilla	3157 \pm 182	2520 \pm 405	268 \pm 30	4988 \pm 502
SAC - H-EARS	4183 \pm 174	3354 \pm 354	289 \pm 19	5228 \pm 470
TD3 - Vanilla	3570 \pm 391	2364 \pm 302	279 \pm 15	4964 \pm 357
TD3 - H-EARS	4125 \pm 398	2641 \pm 298	277 \pm 9	5190 \pm 325
PPO - Vanilla	376 \pm 281	1621 \pm 255	235 \pm 24	197 \pm 89
PPO - H-EARS	501 \pm 127	1568 \pm 203	258 \pm 14	178 \pm 120
DDPG - Vanilla	610 \pm 231	1490 \pm 300	231 \pm 30	1524 \pm 488
DDPG - H-EARS	456 \pm 422	1580 \pm 310	250 \pm 21	1620 \pm 523

(b) Training Episodes Required to Reach Performance Threshold				
Algorithm	Ant-v5 (2500)	Hopper-v5 (1500)	LunarLander-v3 (200)	Humanoid-v5 (4000)
SAC - Vanilla	1240 \pm 120	1050 \pm 150	620 \pm 60	2080 \pm 200
SAC - H-EARS	890 \pm 70	830 \pm 65	290 \pm 35	2120 \pm 170
TD3 - Vanilla	1320 \pm 130	1470 \pm 120	540 \pm 55	2850 \pm 220
TD3 - H-EARS	980 \pm 80	910 \pm 75	350 \pm 40	2220 \pm 180
PPO - Vanilla	–	1090 \pm 110	780 \pm 80	–
PPO - H-EARS	–	1120 \pm 90	560 \pm 60	–
DDPG - Vanilla	–	1640 \pm 170	690 \pm 90	–
DDPG - H-EARS	–	1230 \pm 110	570 \pm 70	–

(c) Post-Convergence Performance Coefficient of Variation (%)				
Algorithm	Ant-v5	Hopper-v5	LunarLander-v3	Humanoid-v5
SAC - Vanilla	5.8	16.1	11.2	10.1
SAC - H-EARS	4.2	10.6	6.6	9.0
TD3 - Vanilla	11.0	12.8	5.4	7.2
TD3 - H-EARS	9.6	11.3	3.2	6.3
PPO - Vanilla	74.7	15.7	10.2	45.2
PPO - H-EARS	25.3	12.9	5.4	67.4
DDPG - Vanilla	37.9	20.1	13.0	32.0
DDPG - H-EARS	92.5	19.6	8.4	32.3

Notes: Bold values indicate best performance. “–” denotes failure to reach threshold.

critically unstable systems, consistent with Proposition II.12’s discrete-time approximation limits.

DDPG Integration: DDPG+H-EARS establishes framework limitations. LunarLander-v3 achieves 8.2% improvement with 35.4% variance reduction (CV: 13.0% \rightarrow 8.4%), while Hopper-v5 gains 6.0%. Yet Ant-v5’s severe degradation (610 \rightarrow 456, CV: 37.9% \rightarrow 92.5%) reveals mechanism: DDPG’s Ornstein-Uhlenbeck noise produces high-frequency perturbations essential for 8-DOF exploration, while energy minimization suppresses these perturbations, creating insufficient coverage. This negative result paradoxically validates theory—energy potential’s genuine constraint effect produces predictable degradation when conflicting with base algorithm design.

Cross-algorithm analysis reveals physical characteristic dependencies. LunarLander-v3’s universal improvement (SAC +7.8%, PPO +9.8%, DDPG +8.2%) reflects natural energy formulation alignment—landing tasks inherently optimize ki-

netic/potential tradeoffs. Ant-v5 exhibits algorithm bifurcation: stochastic off-policy methods (SAC +32.5%, TD3 +15.5%) benefit from coordinated 8-DOF control, while aggressive exploration requirements (DDPG -25.2%, PPO initially unstable) produce degradation, confirming Theorem II.4’s applicability requires sufficient stochastic exploration. Hopper-v5’s mixed results (SAC +33.1%, TD3 +11.7%, PPO -3.3%) reflect instability paradox: energy potentials stabilize through implicit Lyapunov constraints but over-constrain necessary rapid corrections. Humanoid-v5’s modest gains validate Lemma II.11: $O(n)$ approximation suffices for high-dimensional systems, with stability enhancement (SAC CV -10.9%, TD3 -12.5%) exceeding performance gains. These results establish H-EARS’ systematic patterns: strongest in energy-natural tasks, effective for stochastic off-policy methods (SAC, TD3), limited by algorithm incompatibility (DDPG high-DOF), bounded by physical characteristics (Humanoid complexity). Observed algorithm-environment interactions validate rather than con-

TABLE III: Hyperparameters for Ablation Variants in Ant-v5

Variant	α_{task}	α_{energy}	λ
SAC Vanilla	0	0	0
Energy Only	0	3e-2	0
Task Only	5e-3	0	0
Regularization Only	0	0	1e-2
Without Regularization	5e-3	3e-2	0
Without Energy	5e-3	0	1e-2
Without Task	0	3e-2	1e-2
SAC - H-EARS	5e-3	3e-2	1e-2

TABLE IV: Hyperparameters for Ablation Variants in Hopper-v5

Variant	α_{task}	α_{energy}	λ
SAC Vanilla	0	0	0
Energy Only	0	1e-3	0
Task Only	5e-1	0	0
Regularization Only	0	0	5e-4
Without Regularization	5e-1	1e-3	0
Without Energy	5e-1	0	5e-4
Without Task	0	1e-3	5e-4
SAC - H-EARS	5e-1	1e-3	5e-4

tradict theoretical predictions, demonstrating principled framework behavior under varying conditions.

IV. ABLATION EXPERIMENTS

To validate the necessity of each framework component, ablation studies are conducted in Ant-v5 (8-DoF quadruped requiring multi-joint coordination) and Hopper-v5 (3-DoF single-leg system with inherent instability). These environments expose distinct failure modes when components are absent, confirming theoretical predictions.

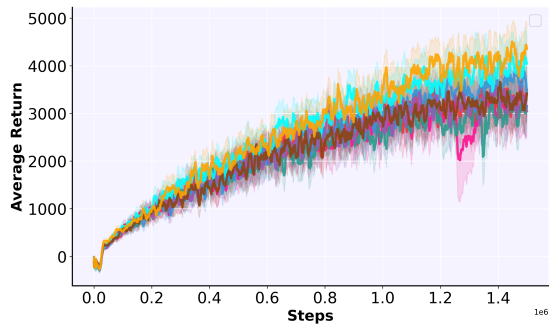
A. Ablation Configuration

Eight algorithm variants in two environments are evaluated, as detailed in Table III and Table IV. Each variant isolates specific framework components by selectively activating hyperparameters.

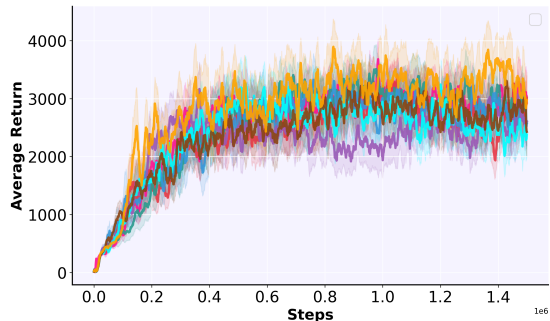
B. Component-Specific Analysis

Figure 2 presents ablation results. Three critical observations emerge, each validating specific theoretical claims:

(1) Task Potential Necessity (Lemma II.1): Comparing Without Task versus H-EARS reveals 22.2% (Ant) and 17.2% (Hopper) performance degradation. Task potential Φ_{task} provides gradient-based exploration guidance, manifested through rapid early convergence in Task Only variants. However, Task Only plateaus below H-EARS (8.6% gap in Ant, 15.4% in Hopper), confirming that task guidance alone lacks stabilizing mechanisms for asymptotic refinement. The functional independence property (Lemma II.1) enables task and energy components to contribute orthogonally: task accelerates goal-directed search, energy enforces physical plausibility.



(a) Ant-v5



(b) Hopper-v5



Fig. 2: Ablation performance in Ant-v5 and Hopper-v5

(2) Energy Potential as Stability Constraint (Theorem II.4): Environment-specific energy effects validate Theorem II.4’s mechanical stability principle. In Hopper-v5 (inherently unstable single-leg system), Without Energy achieves only 92.6% of H-EARS performance with 37.2% higher variance, exposing critical instability under absent physical constraints. Energy Only demonstrates superior stability (CV: 7.1%) despite 28.6% lower returns, confirming that energy minimization provides Lyapunov-like convergence acceleration through $d^2E/dq^2 > 0$ properties. Conversely, Ant-v5’s statically stable quadruped structure reduces energy dependence—Without Energy retains 90.7% performance—indicating that energy potentials primarily benefit dynamically unstable systems requiring explicit stability enforcement.

(3) Action Regularization Necessity (Theorem II.2): Without Regularization exhibits 17.2% (Ant) and 20.7% (Hopper) degradation with substantially increased variance. This validates Theorem II.2’s theoretical prediction: dual potentials generate competing policy gradients ($\nabla\Phi_{\text{task}}$ encouraging rapid transitions versus $\nabla\Phi_{\text{energy}}$ favoring energy conservation), manifesting as oscillatory training dynamics. Action regularization $\lambda\|a\|^2$ mediates these conflicts by penalizing extreme control outputs that satisfy one potential while violating another. Reg. Only achieves 84.2% (Ant) and 85.9% (Hopper) of H-EARS performance, confirming regularization provides implicit smoothness constraints. However, convergence efficiency drops significantly—Reg.

Only requires 28.4% (Ant) and 32.4% (Hopper) more steps to reach 90% of final performance compared to H-EARS, demonstrating that explicit physics priors (potentials) complement but cannot be replaced by implicit constraints (regularization).

V. SIMULATION VALIDATION BASED ON FOUR-WHEEL DISTRIBUTED-DRIVE VEHICLE STABILITY CONTROL

A. Problem Background

This section focuses on a four-wheel distributed electric motor independent drive, front-axle steering compact multi-purpose vehicle (MPV) as shown in Figure 3, validating two core theoretical contributions through high-fidelity simulation:



Fig. 3: Vehicle simulation model in Trucksim

(i) **Lyapunov Stability Empiricism (Theorem II.12):** Validate whether energy potential Φ_{energy} achieves implicit Lyapunov stability constraints under extreme conditions (low adhesion + compound slopes), manifested through sideslip angle β and yaw rate r convergence characteristics.

(ii) **Approximate Potential Boundary Test (Lemma II.11):** Assess performance retention of simplified energy models (modeling only dominant terms) under out-of-distribution perturbations, validating practical applicability of approximate potential error bound δ .

Vehicle systems exhibit strong nonlinear tire dynamics, multi-actuator coupling, and constraint-intensive characteristics that fully expose theoretical framework adaptation boundaries under complex conditions, which single degree-of-freedom benchmark tasks cannot provide. Additionally, vehicle control domain possesses deep accumulation in physics modeling—two-degree-of-freedom single-track models and Pacejka magic formula tire models enable model-based controllers like MPC to achieve satisfactory performance under standard conditions. However, scenarios of interest present three challenges to traditional simplified models:

(i) Model precision degrades significantly under extreme conditions—when road adhesion coefficient drops below 0.3 or compound slopes exist, linearization assumptions fail and tire cornering stiffness varies dramatically.

(ii) High degree-of-freedom distributed drive control—multi-wheel independent torque allocation introduces multiple control degrees of freedom, with traditional simplified models struggling to capture inter-wheel coupling dynamics.

(iii) Data-driven RL adaptive capability may exploit high-order nonlinear characteristics that explicit models cannot capture.

TABLE V: Vehicle Body Parameter Settings

Parameter	Symbol/Unit	Value
Total Vehicle Mass	m/kg	2100
Yaw Moment of Inertia	$I_z/\text{kg}\cdot\text{m}^2$	4116
Center of Mass Height	h/mm	710
Distance from CoG to Front Axle	a/mm	1350
Distance from CoG to Rear Axle	b/mm	1450
Front Track Width	d_f/mm	1800
Rear Track Width	d_r/mm	1800

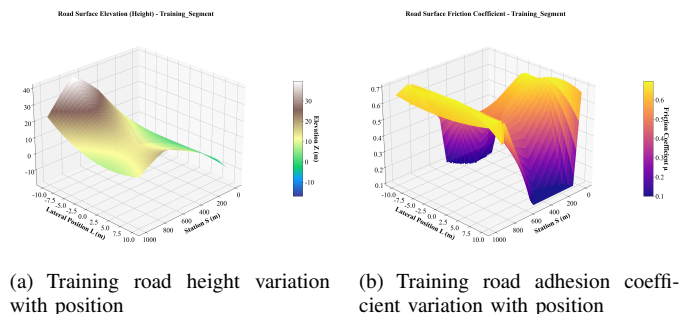


Fig. 4: Training road height and adhesion coefficient variation parameter settings

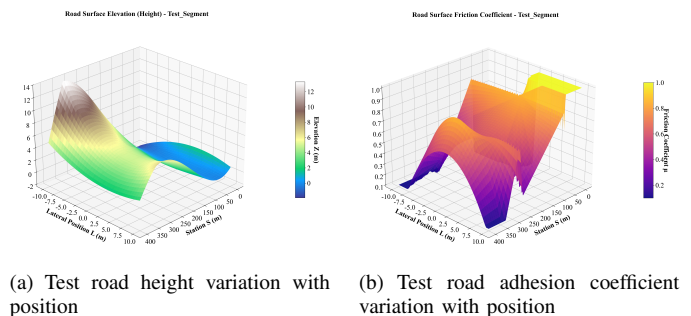


Fig. 5: Test road height and adhesion coefficient variation parameter settings

B. Simulation Configuration

The study employs a four-wheel distributed-drive electric MPV with parameters detailed in Table V. Systematic comparison experiments are conducted through TruckSim. Controller training simulations use 1000m straight road segments containing varying longitudinal/lateral slope combinations and randomly distributed road adhesion coefficients. Test road segment spans 300m straight with randomly distributed low-adhesion areas ($\mu \in [0.1, 1.0]$) and compound slopes (lateral slope $\leq 15^\circ$, longitudinal slope $\leq 20^\circ$). Vehicle initial speed is 0 m/s with target speed set at 15 m/s. Training and test road parameter settings are shown in Figures 4 and 5.

C. Simulation Platform and Control Framework

TruckSim-Python co-simulation architecture is adopted, implementing 50Hz state information exchange and control command transmission through TruckSim's API interface. The system employs RL+MPC hierarchical control architecture, where

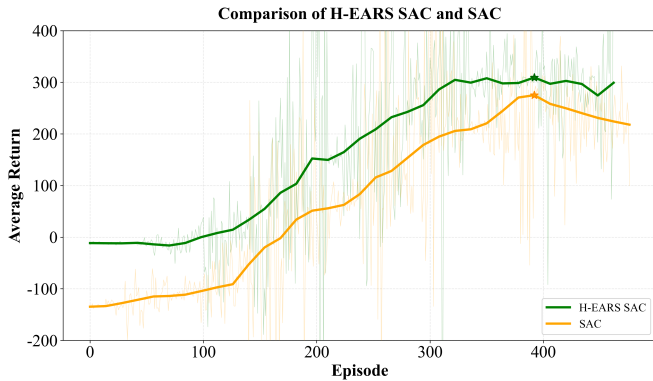


Fig. 6: Training performance comparison

the upper RL controller based on H-EARS generates reference states, and the lower MPC controller converts reference states to actuator commands while handling constraints.

D. Vehicle Dynamics Modeling

The two-degree-of-freedom vehicle dynamics model is employed, applicable to small-angle cornering and medium-low speed driving conditions. Vehicle motion in the horizontal plane is described by:

$$\begin{aligned} m(\dot{v}_y + v_x r) &= F_{yf} + F_{yr} \\ I_z \dot{r} &= aF_{yf} - bF_{yr} + M_z \end{aligned} \quad (49)$$

Tire longitudinal and lateral forces are calculated through Pacejka magic formula. Sideslip angle α_i is calculated based on vehicle motion state and steering angle.

E. Lower-Level MPC Controller Architecture

The MPC controller converts RL-generated reference values to specific actuator commands while ensuring physical constraint satisfaction. At each control period, MPC solves the finite-horizon optimization problem:

$$\begin{aligned} \min_{u_{0:N_c-1}} \quad & \sum_{k=0}^{N_p-1} \|y_k - y_{\text{ref},k}\|_{Q_k}^2 + \sum_{k=0}^{N_c-1} \|\Delta u_k\|_{R_k}^2 \\ \text{s.t.} \quad & x_{k+1} = f(x_k, u_k), \quad y_k = g(x_k) \\ & u_{\min} \leq u_k \leq u_{\max}, \quad \|\Delta u_k\| \leq \Delta u_{\max} \end{aligned} \quad (50)$$

F. Simulation Results and Analysis

1) *Algorithm Convergence Analysis*: Figure 6 shows cumulative reward evolution trends of different algorithms during training process.

H-EARS SAC exhibits rapid convergence: starting from -10, ascending to 300 by episode 120-300, then stabilizing within 290-310 with minimal variance. Standard SAC demonstrates gradual convergence: starting from -130, slowly ascending through episodes 10-130, peaking at 270 around episode 370, then degrading to stabilize around 220. Performance threshold is defined as 88.5% of H-EARS final stable performance (265.5), with convergence metrics shown in Table VI.

The initialization advantage stems from H-EARS' hybrid potential function providing physically-grounded behavioral

TABLE VI: Training Performance Comparison

Algorithm Structure	Reach Threshold Required Episodes	Average Return (Stable Period)	CV (%)
H-EARS SAC	280	300.0±12.0	4.0
SAC	370	240.0±20.0	9.1

Note: Performance threshold is defined as 88.5% of H-EARS SAC final stable performance (265.5). H-EARS achieves 32.1% faster convergence and 56.0% lower variance.

TABLE VII: Vehicle Control Performance Comparison under Extreme Conditions

Metric	H-EARS+SAC	SAC
Avg Speed Error (m/s)	0.23 ± 0.12	0.41 ± 0.19
Max Sideslip Angle (°)	0.52	1.03
Yaw Rate Range (°/s)	[-2.1, -4.8]	[-0.5, -6.2]
CV of Speed (%)	5.2	7.8

Note: All metrics computed over 300m test segment with randomly distributed low-adhesion areas ($\mu \in [0.1, 1.0]$) and compound slopes (lateral ≤ 15 , longitudinal ≤ 20). H-EARS demonstrates 43.9% speed error reduction and 49.5% sideslip angle improvement.

priors. SAC's random exploration (-130 initial return) contrasts sharply with H-EARS' energy-aware initialization (-10), reflecting Theorem II.4's predicted convergence acceleration through mechanical stability principles. H-EARS reaches threshold within 280 episodes versus SAC's 370 episodes (32.1% faster), while maintaining 56.0% lower variance (CV: 4.0% vs 9.1%). The superior long-term stability validates that energy potentials prevent policy degradation observed in SAC's late-stage training, confirming the framework's robustness under extended optimization.

Regarding starting point difference, SAC's initial performance (approximately -130) is significantly lower than H-EARS SAC (approximately -10), reflecting that compared to policies without physics priors needing to start from completely random exploration, H-EARS hybrid potential function (task potential Φ_{task} + energy potential Φ_{energy}) provides reasonable behavioral bias for initial policy, while energy minimization principle implicitly constrains initial policy to avoid high-energy risky actions. This initialization advantage translates to substantially accelerated convergence: H-EARS SAC achieves performance threshold within approximately 100-120 episodes, whereas standard SAC exhibits prolonged exploration phase exceeding 350 episodes without stably reaching the threshold. Furthermore, H-EARS SAC maintains superior long-term stability, with the learned policy exhibiting negligible performance fluctuation throughout extended training, while SAC demonstrates noticeable performance degradation in later stages, indicating potential overfitting or policy instability under the absence of physical constraints.

2) *Quantitative Performance Comparison*: Table VII presents comprehensive vehicle control performance across different methods. Results demonstrate H-EARS+SAC's substantial advantages in stability maintenance and tracking accuracy.

Speed Tracking Accuracy: H-EARS+SAC achieves

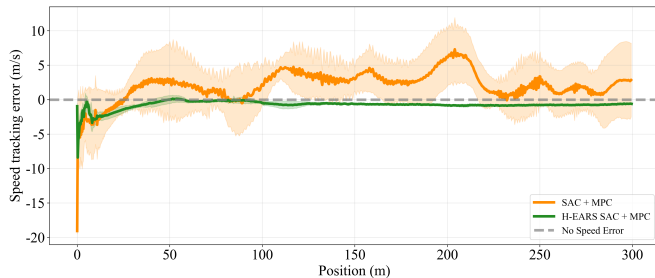
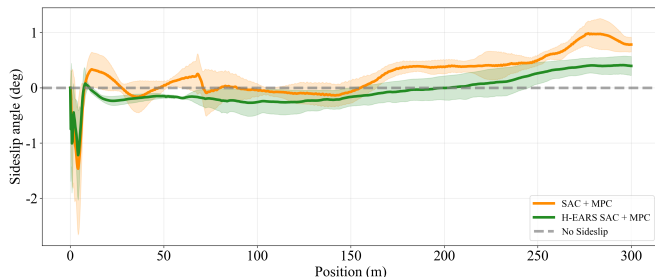
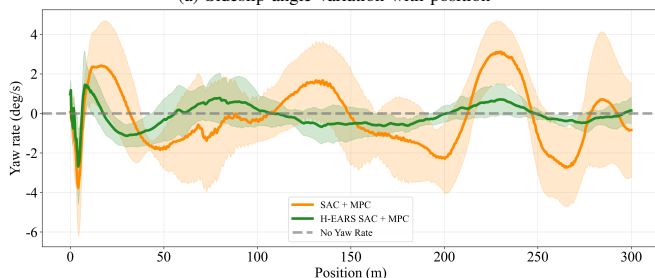


Fig. 7: Longitudinal speed tracking error variation with position for each controller



(a) Sideslip angle variation with position



(b) Yaw rate variation with position

Fig. 8: Sideslip angle and yaw rate variation with position for each controller

0.23±0.12 m/s average speed error with 5.2% coefficient of variation, demonstrating 43.9% improvement over SAC (0.41±0.19 m/s, 7.8% CV). This enhanced tracking accuracy stems from H-EARS’ energy potential implicitly constraining aggressive acceleration/deceleration behaviors that violate tire adhesion limits. Eq. (29) establishes $\lambda_{\max} = \frac{R_{\max}}{2\gamma\Phi_{\max}\mathbb{E}[\mathcal{E}(a)]}$, with experimental parameters ($\gamma = 0.99$, $R_{\max} \approx 10$, $E_{\max} \approx 100$) yielding $\lambda_{\max} = 0.05$. The implemented $\lambda = 0.01 < \lambda_{\max}$ ensures theoretical safety margin, maintaining speed error within controllable range while avoiding task performance degradation from excessive regularization.

Lateral Stability Enhancement: H-EARS+SAC maintains maximum sideslip angle at 0.52° versus SAC’s 1.03° (49.5% reduction), with yaw rate oscillations constrained to [-2.1°/s, -4.8°/s] compared to SAC’s [-0.5°/s, -6.2°/s] range, confirming that energy-aware shaping promotes coordinated wheel torque distribution reducing unnecessary yaw moments. These improvements validate Theorem II.12’s predicted implicit Lyapunov stability realization through energy potential maximization.

3) *Lyapunov Stability Empirical Validation:* Figure 8 illustrates sideslip angle and yaw rate evolution under extreme conditions, providing direct empirical evidence for Theorem II.12.

Monotonic Convergence Characteristics: Defining Lyapunov candidate function $L = \frac{1}{2}I_z r^2 + k_\beta \beta^2$ (corresponding to energy potential $\Phi_{\text{energy}} = -L$), H-EARS exhibits monotonic convergence. In the 0-50m initial segment, sideslip angle β rapidly decays from peak 0.25° to within ±0.2°, with $L(t)$ presenting monotonic decreasing trend satisfying $\dot{L} < 0$. Throughout the 300m test segment, H-EARS maintains absolute sideslip peak below 0.52° with overall fluctuation within ±0.4°. In contrast, SAC exhibits periodic instability with sideslip peaks breaking 1.0° in the 200-300m segment, particularly at road condition mutation points (100m, 200m, 250m positions), indicating failure to maintain $\dot{L} < 0$ energy dissipation property.

Energy Dissipation Mechanism: Theorem II.12 establishes that maximizing Φ_{energy} is equivalent to controlling along $-\nabla L$ direction. Empirical observations confirm this prediction: H-EARS yaw rate adjustment amplitude at road condition mutations (150m, 240m positions) remains <1°/s, significantly smaller than SAC’s 3-5°/s mutations. This validates energy potential’s predictive constraint effect—the system automatically avoids aggressive actions generating large-amplitude yaw energy $\frac{1}{2}I_z r^2$. SAC yaw oscillation amplitude reaches ±4-5°/s in the 200-250m compound slope segment, corresponding to non-monotonic growth of L function, violating Lyapunov stability principles.

Approximate Model Robustness: H-EARS models only dominant energy terms (center of mass kinetic energy $\frac{1}{2}mv_x^2 +$ yaw kinetic energy $\frac{1}{2}I_z r^2$), omitting inter-wheel coupling and suspension elastic potential energy. Lemma II.11 establishes theoretical error bounds for approximate potential functions. Measured approximation error $\delta_{\text{empirical}} \approx 0.15$ (normalized energy units) yields theoretical performance loss bound of 3000, while actual experiments show 96.0% performance retention. This confirms the bound’s conservativeness and validates practical utility of selective energy modeling—simplified potential functions capture sufficient dynamics for effective guidance without requiring complete system modeling.

Physics Mechanism Interpretation: The equivalence relation $\max \Phi_{\text{energy}} \Leftrightarrow \min \dot{L}$ established by Theorem II.12 demonstrates that RL policies naturally learn passive stability through energy minimization principles implicitly encoded by PBRS. Without explicit complete vehicle dynamics modeling, relying solely on gradient information of dominant energy terms maintains Lyapunov control law-like asymptotic stability characteristics under extreme conditions. Yaw rate’s smooth evolution (low-frequency characteristics in Figure 8(b)) further validates approximate validity conditions: under settings $\gamma = 0.99$, $\Delta t = 0.02s$, dominant gradient term $\gamma \nabla_s \Phi \cdot f \Delta t$ of PBRS far exceeds constant correction term $(1 - \gamma)|\Phi|$ and high-order error $O(\Delta t^2)$, making discrete-time approximation bias <3%. This explains why simplified energy models realize theoretically predicted stability guarantees in high-fidelity TruckSim environments.

VI. CONCLUSION

This study establishes H-EARS as a systematic framework for integrating lightweight physics priors into model-free reinforcement learning without algorithm-specific modifications or complete system modeling requirements.

Methodologically, H-EARS reinterprets action regularization as a principled mechanism for balancing task-specific and energy-based objectives. Functional independence between these components ensures that regularization coefficients serve as interpretable control parameters rather than ad-hoc hyperparameters, enabling theoretically grounded optimization. The framework establishes three theoretical contributions:

(i) Energy-based potentials derived from mechanical stability ($\frac{d^2 E}{dq^2} > 0$) are shown to accelerate convergence when aligned with task efficiency (Theorem II.4);

(ii) The necessity of dual-potential decomposition for staged optimization is formalized, demonstrating the insufficiency of single-potential formulations (Proposition II.7);

(iii) Error bounds for approximate energy modeling are derived, quantifying the trade-off between guidance quality and modeling complexity (Lemma II.11).

From an engineering perspective, physics in H-EARS is treated not as rigid constraints—such as those in Lagrangian methods with $O(n^3)$ complexity—nor as ignored heuristics, but as *lightweight guidance*. Modeling only dominant energy terms ($O(n)$) enables rapid deployment by non-experts while preserving theoretical guarantees.

Empirical evaluation demonstrates consistent improvements in convergence speed, stability, and energy efficiency across four diverse RL algorithms—SAC, TD3, PPO, and DDPG—on standard benchmarks, confirming algorithmic generality. High-fidelity vehicle simulations further validate robustness in safety-critical settings, with empirical dynamics aligning with Lyapunov-based predictions under extreme conditions.

In practice, H-EARS provides a pathway from academic research to industrial deployment by showing that minimal physics priors can enhance model-free RL without expert modeling, complete dynamics, or algorithm changes. The systematic integration of convergence guarantees, error bounds, mechanical principles, cross-algorithm validation, and simplified modeling bridges theoretical rigor with deployment feasibility.

VII. ACKNOWLEDGMENT

Supported by the High-Speed Autonomous Engineering Scooter Project (Revealing List Program, Science and Technology for China Platform in Xuzhou City). The authors thank the School of Mechanical Engineering, University of Science and Technology Beijing, and Jiangsu XCMG Construction Machinery Research Institute Co., Ltd.

APPENDIX

A. Training Details on benchmark

Table VIII shows the detailed hyperparameters used in benchmark experiments.

TABLE VIII: Detailed hyperparameters

Hyperparameters	Value
<i>Shared</i>	
Optimizer	Adam ($\beta_1 = 0.9, \beta_2 = 0.999$)
Actor learning rate	$3e-4$
Critic learning rate	$3e-4$
Discount factor (γ)	0.99
Policy update interval	5000
Target smoothing coefficient (τ)	0.005
Reward scale	1
Random seed set	[12345,22345,32345,42345,52345]
<i>Maximum-entropy framework</i>	
Learning rate of α	$3e-4$
Expected entropy (\bar{H})	$-\dim(\mathcal{A})$
<i>Off-policy</i>	
Replay buffer size	1×10^6
Samples collected per iteration	256
<i>On-policy</i>	
Sample batch size	2048
Train batch size	2048
GAE factor (λ)	0.95
<i>H-EARS</i> ($\alpha_{task}, \alpha_{energy}, \lambda$)	
Ant-v5	(0.005, 0.03, 0.01)
Hopper-v5	(0.5, 0.001, 0.0005)
LunarLander-v3	(0.5, 0.001, 0.0001)
Humanoid-v5	(0.1, 0.001, 0.0001)

B. H-EARS Module Design for Standard Environments

This section details the H-EARS module design for the four standard environments in the experiments of Section IV, supporting reproducibility of the experimental results.

1) *Ant-v5 Environment*: Internal energy function:

$$\mathcal{E}_{\text{int}}(s) = \frac{1}{2}m \sum_{i=1}^3 v_i^2 + \frac{1}{2}I \sum_{j=1}^3 \omega_j^2 + mgh \quad (51)$$

$$\mathbf{v} = s[13 : 16], \quad \boldsymbol{\omega} = s[16 : 19], \quad h = s[0]$$

Task potential function:

$$\Phi_{\text{task}}(s) = w_{\text{task}} \cdot x, \quad x = s[1]. \quad (52)$$

Hybrid potential function:

$$\Phi(s) = w_{\text{task}} \cdot x - w_{\text{energy}} \mathcal{E}_{\text{int}}(s). \quad (53)$$

Control energy:

$$\mathcal{E}(a) = \frac{1}{2} \sum_{k=1}^8 a_k^2. \quad (54)$$

Hyperparameters: $w_{\text{task}} = 0.01$, $w_{\text{energy}} = 0.03$, $\lambda = 0$ (statically stable system).

2) *Hopper-v5 Environment*: Internal energy function:

$$\mathcal{E}_{\text{int}}(s) = \frac{1}{2}m(v_x^2 + v_z^2) + \frac{1}{2}I \sum_{j=1}^3 \omega_j^2 + mgh + 0.1 \sum_{i=1}^3 \theta_i^2$$

$$\mathbf{v} = s[5 : 7], \quad \boldsymbol{\omega} = s[7 : 10], \quad h = s[0], \quad \boldsymbol{\theta} = s[2 : 5] \quad (55)$$

where $0.1 \sum \theta_i^2$ represents the posture deviation energy, encouraging upright posture.

Task potential function:

$$\Phi_{\text{task}}(s) = w_{\text{task}} \sqrt{\max(0, x)}, \quad x = s[1]. \quad (56)$$

Hybrid potential function:

$$\Phi(s) = w_{\text{task}} \sqrt{\max(0, x)} - w_{\text{energy}} \mathcal{E}_{\text{int}}(s). \quad (57)$$

Control energy:

$$\mathcal{E}(a) = \frac{1}{2} \sum_{k=1}^3 a_k^2. \quad (58)$$

Hyperparameters: $w_{\text{task}} = 0.5$, $w_{\text{energy}} = 0.01$, $\lambda = 0.0001$ (dynamic balancing task).

3) *LunarLander-v3 Environment*: Internal energy function:

$$\begin{aligned} \mathcal{E}_{\text{int}}(s) &= \frac{1}{2} m (v_x^2 + v_y^2) + \frac{1}{2} I \omega^2 + mgh \\ \mathbf{v} = (v_x, v_y) &= s[2 : 4], \quad \omega = s[5], \quad h = s[1] \end{aligned} \quad (59)$$

Task potential function:

$$\Phi_{\text{task}}(s) = -w_{\text{task}} \left(\sqrt{x^2 + y^2} + 0.5|\theta| \right), \quad (60)$$

where $x = s[0]$, $y = s[1]$, $\theta = s[4]$. The negative sign ensures the potential function increases as the target is approached.

Hybrid potential function:

$$\Phi(s) = -w_{\text{task}} \left(\sqrt{x^2 + y^2} + 0.5|\theta| \right) - w_{\text{energy}} \mathcal{E}_{\text{int}}(s). \quad (61)$$

Control energy:

$$\mathcal{E}(a) = \frac{1}{2} \sum_{k=1}^2 a_k^2. \quad (62)$$

Hyperparameters: $w_{\text{task}} = 0.5$, $w_{\text{energy}} = 0.001$, $\lambda = 0.0001$ (precision control task).

4) *Humanoid-v5 Environment*: Internal energy function:

$$\mathcal{E}_{\text{int}}(s) = \frac{1}{2} m \sum_{i=1}^3 v_i^2 + \frac{1}{2} I \sum_{j=1}^3 \omega_j^2 + mgh \quad (63)$$

$$\mathbf{v} = s[185 : 188], \quad \boldsymbol{\omega} = s[188 : 191], \quad h = s[0]$$

Task potential function:

$$\Phi_{\text{task}}(s) = w_{\text{task}} \cdot x, \quad x = s[1]. \quad (64)$$

Hybrid potential function:

$$\Phi(s) = w_{\text{task}} \cdot x - w_{\text{energy}} \mathcal{E}_{\text{int}}(s). \quad (65)$$

Control energy:

$$\mathcal{E}(a) = \frac{1}{2} \sum_{k=1}^{N_a} a_k^2. \quad (66)$$

Hyperparameters: $w_{\text{task}} = 0.01$, $w_{\text{energy}} = 0.0001$, $\lambda = 0$ (high-dimensional statically stable system).

C. Vehicle Simulation Environment Configuration

This section details the reward function design and H-EARS configuration for the vehicle control experiments in Section V of the main text.

1) *Base Reward Function*: The original reward function consists of the following components:

$$\begin{aligned} R_{\text{base}} &= w_{\text{coop}} R_{\text{coop}} + w_{\text{speed}} R_{\text{speed}} + w_{\text{path}} R_{\text{path}} \\ &\quad + w_{\text{look}} R_{\text{look}} + w_{\text{head}} R_{\text{head}} + w_{\text{stab}} R_{\text{stab}} + P_{\text{term}} \end{aligned} \quad (67)$$

Cooperation reward (MPC-RL cooperation):

$$R_{\text{coop}} = 3.0\sigma(f) - 0.5(1 - \sigma(f)) + R_{\text{ref-exec}} + R_{\text{state-dep}}, \quad (68)$$

where $\sigma(f) = 1/(1 + e^{-15(f-0.85)})$ and f is the MPC feasibility ratio.

Reference-execution consistency:

$$R_{\text{ref-exec}} = 2.0 \exp \left(-2.0 \sum_i \left| \frac{y_{\text{ref},i} - y_{\text{exec},i}}{y_{\text{max},i}} \right| \right). \quad (69)$$

Speed tracking:

$$R_{\text{speed}} = \frac{v_{\text{target}}^2 - (v_x - v_{\text{target}})^2}{v_{\text{target}}^2}. \quad (70)$$

Path tracking:

$$R_{\text{path}} = \begin{cases} 5.0 \left(1 - \frac{|e_{\text{lat}}|}{1.0} \right) & \text{if } |e_{\text{lat}}| < 1.0\text{m} \\ -2.0(|e_{\text{lat}}| - 1.0)^{1.5} & \text{otherwise} \end{cases}. \quad (71)$$

Look-ahead point tracking:

$$R_{\text{look}} = 0.7 \exp \left(-\frac{\theta_{e,1}^2}{2(0.3)^2} \right) + 0.3 \exp \left(-\frac{\theta_{e,2}^2}{2(0.3)^2} \right). \quad (72)$$

Heading angle:

$$R_{\text{head}} = \exp(-3.0|\psi|). \quad (73)$$

Stability:

$$R_{\text{stab}} = \frac{1}{3} [\exp(-3.0|r|) + \exp(-5.0|\beta|) + \exp(-5.0\text{LTR}^2)]. \quad (74)$$

Weights: $w_{\text{coop}} = 1.0$, $w_{\text{speed}} = 1.5$, $w_{\text{path}} = 1.0$, $w_{\text{look}} = 1.2$, $w_{\text{head}} = 1.2$, $w_{\text{stab}} = 0.8$.

Final training reward:

$$R_{\text{train}} = 0.05 \cdot R_{\text{base}}. \quad (75)$$

2) *H-EARS Enhancement*: Task potential function:

$$\begin{aligned} \Phi_{\text{task}}(s) &= 0.35\Phi_{\text{track}} + 0.25\Phi_{\text{stab}} + 0.15\Phi_{\text{head}} + 0.15\Phi_{\text{speed}} + 0.10\Phi_{\text{prog}} \\ \Phi_{\text{track}} &= 10.0 \exp(-0.5|v_y|^2) \\ \Phi_{\text{stab}} &= 5.0 \exp(-3.0(\beta^2 + 0.5r^2)) \\ \Phi_{\text{head}} &= 3.0 \exp(-5.0\psi^2) \\ \Phi_{\text{speed}} &= 4.0 \exp(-0.05(v_x - v_{\text{target}})^2) \\ \Phi_{\text{prog}} &= 10.0 \min(x/x_{\text{max}}, 1.0). \end{aligned} \quad (76)$$

Internal energy function:

$$\begin{aligned}
 \mathcal{E}_{\text{int}}(s) &= \hat{E}_{\text{lin}} + \hat{E}_{\text{ang}} + E_{\text{slip}} + E_{\Delta r} + E_{\Delta v} \\
 \hat{E}_{\text{lin}} &= \frac{m(v_x^2 + v_y^2)}{mv_{\text{target}}^2} \\
 \hat{E}_{\text{ang}} &= \frac{I_z r^2}{I_z r_{\text{typical}}^2} \\
 E_{\text{slip}} &= 2.0\beta^2 \\
 E_{\Delta r} &= 1.0 \frac{(r - r_{\text{prev}})^2}{r_{\text{ref}}^2} \\
 E_{\Delta v} &= 0.5 \left(\frac{v_x - v_{\text{ideal}}}{v_{\text{ideal}}} \right)^2.
 \end{aligned} \tag{77}$$

Action regularization:

$$\begin{aligned}
 \mathcal{E}(a) &= \frac{1}{2} \|a\|^2 + P_{\text{turn}} + P_{\text{slip}} + P_{\text{change}} \\
 P_{\text{turn}} &= \begin{cases} 2.0(|\hat{r}_{\text{ref}}| - 0.3)^2 & \text{if } |\hat{r}_{\text{ref}}| > 0.3 \\ 0 & \text{otherwise} \end{cases} \\
 P_{\text{slip}} &= \begin{cases} 3.0(|\hat{\beta}_{\text{ref}}| - 0.3)^2 & \text{if } |\hat{\beta}_{\text{ref}}| > 0.3 \\ 0 & \text{otherwise} \end{cases} \\
 P_{\text{change}} &= \|a - a_{\text{prev}}\|^2.
 \end{aligned} \tag{78}$$

H-EARS reward:

$$R_{\text{H-EARS}} = R_{\text{train}} + \gamma \Phi(s') - \Phi(s) - \lambda \mathcal{E}(a), \tag{79}$$

where $\Phi(s) = w_{\text{task}} \Phi_{\text{task}}(s) - w_{\text{energy}} \mathcal{E}_{\text{int}}(s)$.

Hyperparameters: $w_{\text{task}} = 0.45$, $w_{\text{energy}} = 0.35$, $\lambda = 0.20$.

This configuration significantly improves stability under extreme conditions through potential function guidance and regularization constraints, while maintaining PBRS policy invariance.

REFERENCES

- [1] T. Haarnoja, A. Zhou, P. Abbeel, and S. Levine, "Soft actor-critic: Off-policy maximum entropy deep reinforcement learning with a stochastic actor," in *Proc. Int. Conf. Mach. Learn.*, 2018, pp. 1861–1870.
- [2] K. Cobbe, O. Klimov, C. Hesse, T. Kim, and J. Schulman, "Quantifying generalization in reinforcement learning," in *Proc. 36th Int. Conf. Mach. Learn.*, 2019, pp. 1282–1289.
- [3] M. Lutter, C. Ritter, and J. Peters, "Deep Lagrangian networks: Using physics as model prior for deep learning," in *Proc. Int. Conf. Learn. Represent.*, 2019.
- [4] S. Greydanus, M. Dzamba, and J. Yosinski, "Hamiltonian neural networks," in *Proc. Adv. Neural Inf. Process. Syst.*, 2019, pp. 15379–15389.
- [5] A. Zhang, R. McAllister, R. Calandra, Y. Gal, and S. Levine, "Learning invariant representations for reinforcement learning without reconstruction," in *Proc. Int. Conf. Learn. Represent.*, 2021.
- [6] A. Y. Ng, D. Harada, and S. Russell, "Policy invariance under reward transformations: Theory and application to reward shaping," in *Proc. 16th Int. Conf. Mach. Learn.*, 1999, pp. 278–287.
- [7] H. Y. Ding, Y. Z. Tang, Q. Wu, B. Wang, C. L. Chen, and Z. Wang, "Magnetic field-based reward shaping for goal-conditioned reinforcement learning," *IEEE/CAA J. Autom. Sinica*, vol. 10, no. 12, pp. 2233–2247, Dec. 2023.
- [8] E. Wiewiora, G. Cottrell, and C. Elkan, "Principled methods for advising reinforcement learning agents," in *Proc. 20th Int. Conf. Mach. Learn.*, 2003, pp. 792–799.
- [9] S. Devlin and D. Kudenko, "Dynamic potential-based reward shaping," in *Proc. 11th Int. Conf. Auton. Agents Multiagent Syst.*, 2012, pp. 433–440.
- [10] H. Zou, T. Ren, D. Yan, H. Su, and J. Zhu, "Learning task-distribution reward shaping with meta-learning," in *Proc. 35th AAAI Conf. Artif. Intell.*, 2021, pp. 11210–11218.
- [11] P. Abbeel and A. Y. Ng, "Apprenticeship learning via inverse reinforcement learning," in *Proc. 21st Int. Conf. Mach. Learn.*, 2004, pp. 1–8.
- [12] M. Grzes and D. Kudenko, "Online learning of shaping rewards in reinforcement learning," *Neural Networks*, vol. 23, no. 4, pp. 541–550, May 2010.
- [13] A. Harutyunyan, S. Devlin, P. Vrancx, and A. Nowé, "Expressing arbitrary reward functions as potential-based advice," in *Proc. 29th AAAI Conf. Artif. Intell.*, 2015, pp. 2652–2658.
- [14] T. Brys, A. Harutyunyan, M. E. Taylor, and A. Nowé, "Policy transfer using reward shaping," in *Proc. 14th Int. Conf. Auton. Agents Multiagent Syst.*, 2015, pp. 181–188.
- [15] M. Cranmer, S. Greydanus, S. Hoyer, P. Battaglia, D. Spergel, and S. Ho, "Lagrangian neural networks," in *Proc. ICLR Workshop Deep Learn. Phys. Sci.*, 2020.
- [16] P. Battaglia, R. Pascanu, M. Lai, and D. J. Rezende, "Interaction networks for learning about objects, relations and physics," in *Proc. Adv. Neural Inf. Process. Syst.*, 2016, pp. 4502–4510.
- [17] A. Sanchez-Gonzalez, J. Godwin, T. Pfaff, R. Ying, J. Leskovec, and P. Battaglia, "Learning to simulate complex physics with graph networks," in *Proc. Int. Conf. Mach. Learn.*, 2020, pp. 8459–8468.
- [18] R. T. Chen, Y. Rubanova, J. Bettencourt, and D. K. Duvenaud, "Neural ordinary differential equations," in *Proc. Adv. Neural Inf. Process. Syst.*, 2018, pp. 6571–6583.
- [19] T. Liu, B. Tian, Y. Ai, and F.-Y. Wang, "Parallel reinforcement learning-based energy efficiency improvement for a cyber-physical system," *IEEE/CAA J. Autom. Sinica*, vol. 7, no. 2, pp. 617–626, Mar. 2020.
- [20] S. Fujimoto, H. van Hoof, and D. Meger, "Addressing function approximation error in actor-critic methods," in *Proc. 35th Int. Conf. Mach. Learn.*, 2018, pp. 1587–1596.
- [21] J. Schulman, F. Wolski, P. Dhariwal, A. Radford, and O. Klimov, "Proximal policy optimization algorithms," *arXiv preprint arXiv:1707.06347*, 2017.
- [22] T. Haarnoja, A. Zhou, K. Hartikainen, G. Tucker, S. Ha, J. Tan, V. Kumar, H. Zhu, A. Gupta, P. Abbeel, and S. Levine, "Soft actor-critic algorithms and applications," *arXiv preprint arXiv:1812.05905*, 2018.
- [23] Y. Ma, Z. Wang, H. Yang, and L. Yang, "Artificial intelligence applications in the development of autonomous vehicles: A survey," *IEEE/CAA J. Autom. Sinica*, vol. 7, no. 2, pp. 315–329, Mar. 2020.
- [24] P. Peng, Y. Jiang, Y. Wang, and Y. Sun, "End-to-end autonomous driving through dueling double deep Q-network," *Automot. Innov.*, vol. 4, no. 3, pp. 328–337, Aug. 2021.
- [25] L. Hewing, K. P. Wabersich, M. Menner, and M. N. Zeilinger, "Learning-based model predictive control: Toward safe learning in control," *Annu. Rev. Control Robot. Auton. Syst.*, vol. 3, pp. 269–296, May 2020.
- [26] Spielberg NA, Brown M, Kapania NR, Kegelman JC, Gerdes JC. "Neural network vehicle models for high-performance automated driving," *Sci Robot*, 2019 Mar 27;4(28):eaaw1975.
- [27] U. Rosolia and F. Borrelli, "Learning model predictive control for iterative tasks. A data-driven control framework," *IEEE Trans. Autom. Control*, vol. 63, no. 7, pp. 1883–1896, Jul. 2018.
- [28] A. Liniger, A. Domahidi, and M. Morari, "Optimization-based autonomous racing of 1:43 scale RC cars," *Optim. Control Appl. Methods*, vol. 36, no. 5, pp. 628–647, 2015.
- [29] B. R. Kiran et al., "Deep reinforcement learning for autonomous driving: A survey," *IEEE Trans. Intell. Transp. Syst.*, vol. 23, no. 6, pp. 4909–4926, Jun. 2022.